Quantum signal processing for simulating cold plasma waves

I. Novikau [1,*] E. A. Startsev,[1] and I. Y. Dodin [1,2]
[1]*Princeton Plasma Physics Laboratory, Princeton, New Jersey 08543, USA*
[2]*Department of Astrophysical Sciences, Princeton University, Princeton, New Jersey 08544, USA*

(Received 11 December 2021; revised 9 April 2022; accepted 3 June 2022; published 24 June 2022)

Numerical modeling of radio-frequency waves in plasma with sufficiently high spatial and temporal resolution remains challenging even with modern computers. However, such simulations can be sped up using quantum computers in the future. Here, we propose how to do such modeling for cold plasma waves, in particular, for an X wave propagating in an inhomogeneous one-dimensional plasma. The wave system is represented in the form of a vector Schrödinger equation with a Hermitian Hamiltonian. Block encoding is used to represent the Hamiltonian through unitary operations that can be implemented on a quantum computer. To perform the modeling, we apply the so-called quantum signal processing algorithm and construct the corresponding circuit. Quantum simulations with this circuit are emulated on a classical computer, and the results show agreement with traditional classical calculations. We also discuss how our quantum circuit scales with the resolution.

DOI: 10.1103/PhysRevA.105.062444

I. INTRODUCTION

In recent years, there has been a significant development of quantum-computing (QC) applications to simulating classical physical systems. Various methods have been proposed to solve the standard wave equation [1], Poisson's equation [2,3], Maxwell's equations [4,5], first-order linear hyperbolic systems [6], the Navier-Stokes equation [7,8], the Boltzmann equation [9], and to simulate advection-diffusion processes [10]. Recently, it has also been noted [11] that particularly fitting the QC framework may be simulations of the highly dispersive radio-frequency (rf) waves in inhomogeneous classical plasmas, which are of interest due to their rich physics and importance for practical applications. This paper proposes a quantum algorithm for modeling such waves.

A. Introduction to plasma waves

Classical plasmas support a broad variety of waves, which are present there naturally and are also launched with external antennas for plasma diagnostics and control [12]. In the simplest case of cold nonmagnetized plasma, these waves consist of two types. One is the electrostatic Langmuir oscillations of the electron fluid relative to the ion fluid, which occur at the frequency $\omega = \omega_p$, where ω_p is the so-called plasma frequency determined by the local background density (Sec. II A). The other type of wave is electromagnetic light waves, which are similar to the light waves in vacuum but have a different dispersion relation, $\omega = (\omega_p^2 + k^2c^2)^{1/2}$, where $\boldsymbol{k}$ is the wave vector and c is the speed of light. The Langmuir waves have their electric field along $\boldsymbol{k}$, and the light waves have their electric field in the plane perpendicular to $\boldsymbol{k}$; i.e., there are two electromagnetic modes with the same frequency but different polarization. When a background magnetic field $\boldsymbol{B}_0$ is added, the Langmuir and electromagnetic modes hybridize, and also additional branches appear due to the ion motion relative to $\boldsymbol{B}_0$, for example, Alfvén waves at low frequencies. All these branches are classified as O and X waves depending on their polarization, which in the general case is neither strictly parallel nor strictly perpendicular to $\boldsymbol{k}$. Once thermal and kinetic effects are taken into account, even more modes appear (sound waves, electron and ion Bernstein waves, etc.). Even in homogeneous plasma, the number of dispersion branches becomes infinite in this case, and additional modes caused by plasma inhomogeneity are also possible.

In laboratory plasmas such as those in magnetic fusion experiments, the typical frequencies of interest include the ion cyclotron frequencies Ω_i (tens of MHz), lower-hybrid frequency $\omega_{\mathrm{LH}} \sim |\Omega_i\Omega_e|^{1/2}$ (a few GHz), and the electron cyclotron frequency Ω_e ($\sim 10^2$ GHz). The latter is usually comparable to ω_p and to the so-called upper-hybrid (UH) frequency $\omega_{\mathrm{UH}} = (\Omega_e^2 + \omega_p^2)^{1/2}$, at which a collective resonance occurs for $\boldsymbol{k} \perp \boldsymbol{B}_0$. The corresponding waves are widely used to control fusion plasmas through rf heating [13,14] and also current drive [15], which is mainly done with lower-hybrid [16] and electron-cyclotron waves [17] and can also help suppress plasma instabilities [18,19]. Many of these rf techniques are practiced on existing fusion devices [20,21], and current drive in particular is now envisioned to play a large role for achieving steady-state operation and for suppressing instabilities in future devices [22–25]. Hence, precise modeling of rf waves in plasma is of significant practical interest.

Various approximations are used for such modeling, depending on the physics of interest, but for many purposes, the waves can be considered linear and collisions can be neglected. (Quantum effects are entirely negligible for most purposes as well.) Also, the propagation, albeit not absorption, can often be described within the cold fluid approximation. Furthermore, in the "electron frequency range"

*inovikau@pppl.gov

($\omega \sim \Omega_e \sim \omega_p$), ions can be considered stationary; then left of interest are only nondissipative linear oscillations of the electron fluid. Although simplified, this model retains rich wave physics that can be difficult to simulate on a classical computer. The difficulty is due to the fact that the corresponding wavelengths are in the mm range, while the device size is in the meter range. This makes multidimensional simulations computationally expensive [26,27] or even entirely unrealistic. Modeling becomes even more difficult when electromagnetic waves linearly transform into each other or into electrostatic oscillations, which have even smaller wavelengths. (This process is called mode conversion [12,28].) For example, the latter can happen at $\omega \sim \omega_{\mathrm{LH}}$ and $\omega \sim \omega_{\mathrm{UH}}$. Various reduced schemes have been used to speed up simulations of waves in the electron frequency range [29], but they are fundamentally limited. First-principles simulations could be beneficial, and this is where QC could help.

B. Quantum simulations

In this work, we report a quantum algorithm that simulates the propagation of a linear X wave in the electron frequency range in a plasma with an inhomogeneous static magnetic field and inhomogeneous density. The considered problem is one-dimensional, with $\boldsymbol{k} \perp \boldsymbol{B}_0$, in which case the X wave is the branch whose polarization lies in the plane perpendicular to $\boldsymbol{B}_0$. (The remaining O wave has polarization parallel to $\boldsymbol{B}_0$.) We also report test simulations using this algorithm on a classical emulator of a quantum computer. To describe these results, let us introduce the necessary vocabulary first.

We assume the circuit model of quantum computation, where information is stored in a set of n_q quantum bits called *qubits* [30,31]. When entangled, the qubits create a configuration space described by a 2^{n_q}-dimensional complex vector, and such an exponential scaling with n_q can be beneficial in large-dimensional problems. A quantum circuit consists of a sequence of so-called *gates*. Some of the gates operate in parallel, and the longest path between the input and output points of the circuit is called *circuit depth*, which is roughly proportional to the runtime [32]. A gate that acts on m_q qubits can be represented by a $2^{m_q} \times 2^{m_q}$ unitary matrix, while the whole quantum circuit is described by a $2^{n_q} \times 2^{n_q}$ unitary matrix U. This matrix is applied to an initial state $\psi(0)$, generating an output state $\psi(t) = U\psi(0)$, from which classical information is then extracted via a classical measurement. In particular, in this paper we focus on *quantum Hamiltonian simulations* (QHS) of systems with Hermitian Hamiltonians $\mathscr{H}$ that are independent of time t; then, $U = \exp(-i\mathscr{H}t)$.

Here, we bring the X-wave equations to the form suitable for QHS using the analytic model from Ref. [11]. Then, we implement the QHS using the *quantum signal processing* (QSP) paradigm, which was originally developed for efficient QHS [33,34]. The essence of the QSP is in encoding polynomials of given matrices into sequences of rotations. In the QHS in particular, the QSP searches for a polynomial to approximate the exponential function of $\mathscr{H}$, which is *block encoded* into an auxiliary unitary. This state-of-the-art quantum method is now extensively studied in the QC community [35–39] and holds promise as a universal numerical framework applicable to any linear Hamiltonian problem. For instance, it was recently applied to simulations of one-dimensional kinetic plasma waves in the spectral representation [40]. However, an application of the QSP to modeling plasma waves in inhomogeneous plasma, which is a more practical problem, is reported here.

We show that for the problem of our choice, a linear cold-X-wave simulation, the QSP implementing QHS can be constructed efficiently. Using the QuEST computing toolkit [41], we also implement the corresponding circuit explicitly. Then we run this algorithm on a classical emulator of a quantum computer and show that our results agree with those of conventional classical simulations. We also discuss how the resulting QSP quantum circuit scales with the grid resolution, the precision of the QSP approximation, and the simulated time interval.

Our paper is organized as follows. In Sec. II, we outline our analytical model of a linear cold X wave in inhomogeneous plasma and its Schrödinger representation. In Sec. III, we construct the corresponding one-dimensional model and derive the Hamiltonian that is used later in our QHS. It is also shown in Sec. III how to encode the resulting plasma system into a quantum circuit and how to initialize the circuit. The QSP algorithm is explained in Sec. IV, and the block encoding of the wave Hamiltonian is constructed in Sec. V. The comparison of the QSP with classical simulations and the scaling of the QSP circuit are presented in Sec. VI. Finally, the advantages and challenges of applying the QSP to classical plasma problems are discussed in Sec. VII.

II. COLD PLASMA WAVES

A. Basic equations

We assume a cold fluid electron plasma with density $n(\boldsymbol{x})$ immersed into a background magnetic field $\boldsymbol{B}_0(\boldsymbol{x})$. Linear waves in such plasma can be described by the following equations:

$$\partial_t \tilde{\boldsymbol{v}} = -\tilde{\boldsymbol{v}} \times \boldsymbol{B}_0 - \tilde{\boldsymbol{E}}, \tag{1a}$$

$$\partial_t \tilde{\boldsymbol{E}} = n\tilde{\boldsymbol{v}} + \boldsymbol{\nabla} \times \tilde{\boldsymbol{B}}, \tag{1b}$$

$$\partial_t \tilde{\boldsymbol{B}} = -\boldsymbol{\nabla} \times \tilde{\boldsymbol{E}}, \tag{1c}$$

where $\tilde{\boldsymbol{v}}$ is the electron fluid velocity, and $\tilde{\boldsymbol{E}}$ and $\tilde{\boldsymbol{B}}$ are the wave electric and magnetic fields, respectively. Time is measured in units of the maximum plasma frequency $\omega_{p,0} = \omega_p(n_0)$, where $\omega_p(n) = (4\pi n e^2/m)^{1/2}$ is the local plasma frequency (in cgs units), e is the absolute value of the electron charge, m is the electron mass, and n_0 is the maximum value of $n(\boldsymbol{x})$. The velocity is normalized to c, while the fields are normalized to $c\sqrt{4\pi n_0 m}$, and the space coordinate is normalized to $\kappa_x = c/\omega_{p,0}$. Equations (1) satisfy Poynting's theorem

$$\partial_t \int W dV + \int \boldsymbol{N} \cdot d\boldsymbol{S} = 0, \tag{2}$$

where $W = n|\tilde{\boldsymbol{v}}|^2 + |\tilde{\boldsymbol{E}}|^2 + |\tilde{\boldsymbol{B}}|^2$ is the system energy density, and $\boldsymbol{N} = \tilde{\boldsymbol{E}} \times \tilde{\boldsymbol{B}}$ is the Poynting vector. With appropriate boundary conditions (such as the Dirichlet boundary conditions), the integral over the surface $\boldsymbol{S}$ disappears so the total energy $\int W dV$ is conserved.

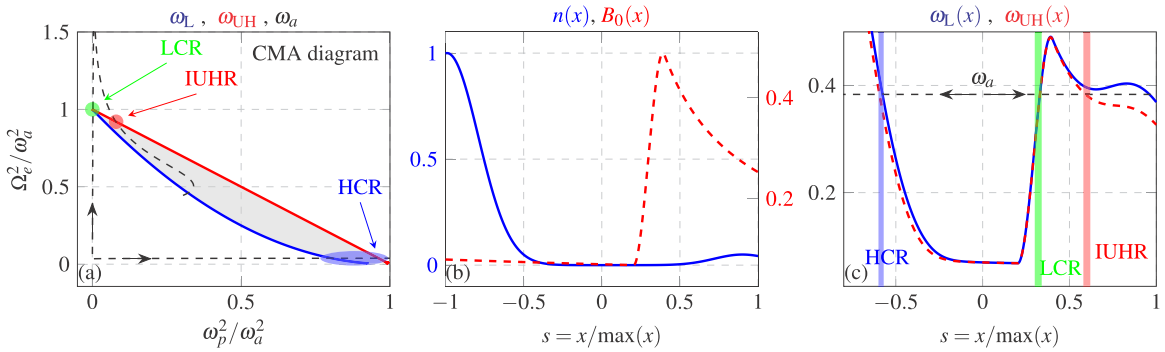

FIG. 1. (a) CMA diagram showing $\omega_L(x)$ (blue bottom solid), $\omega_{UH}(x)$ (red upper solid), and the X-wave frequency ω_a (black dashed) in the parameter space $(\Omega_e^2/\omega_a^2, \omega_p^2/\omega_a^2)$. Here, HCR is the high-density cutoff–resonance pair; LCR is the low-density cutoff–resonance pair; IUHR is an isolated UH resonance. The gray area corresponds to the forbidden zone between the low-density cutoff and the UH resonance. The black arrows indicate the wave propagation from $s = 0$ to $s < 0$ (horizontal arrow) and from $s = 0$ to $s > 0$ (vertical arrow). (b) The corresponding background density $n(x)$ (solid left blue) and magnetic field $B_0(x)$ (red right dashed), Eqs. (44). The peaks in $B_0(x)$ and $n(x)$ at $s > 0$ are added *ad hoc* to reduce wave reflection from the right boundary. They guarantee the presence of the LCR and the IUHR in (a). The parameters of the background profiles are specified in Sec. VI, Eqs. (44a)–(44b). (c) ω_L (solid blue), ω_{UH} (dashed red), and ω_a (dashed black).

One can also rewrite Eqs. (1) as a vector Schrödinger equation [11]

$$\partial_t|\psi\rangle = -i\mathscr{H}|\psi\rangle, \tag{3}$$

where $|\psi\rangle = (\sqrt{n}\tilde{\boldsymbol{v}}, \tilde{\boldsymbol{E}}, \tilde{\boldsymbol{B}})$, and $\mathscr{H}$ serves as a time-independent Hamiltonian, which is Hermitian if the system has suitable boundary conditions (periodic or Dirichlet). The corresponding dynamics is described by

$$|\psi(t)\rangle = e^{-i\mathscr{H}t}|\psi(0)\rangle. \tag{4}$$

Because $\exp(-i\mathscr{H}t)$ is unitary, $\langle\psi|\psi\rangle$ is conserved, which is an alternative representation of Eq. (2) [11].

B. CMA diagram, resonances, and cutoffs

The parameter space of a linear wave with a fixed frequency ω in cold stationary magnetized plasma is fully determined by n and B_0, or equivalently, by ω_p^2/ω^2 and Ω_e^2/ω^2, where $\Omega_e = eB_0/(mc)$ in cgs units. Thus, it is convenient to explore the wave propagation on the plane $(\omega_p^2/\omega^2, \Omega_e^2/\omega^2)$. The corresponding plot is called a Clemmow-Mullaly-Allis (CMA) diagram [12,42]. Notable in this diagram are the curves that correspond to *resonances* and *cutoffs*. Those are defined in the geometrical-optics limit, when the inverse inhomogeneity scale is much smaller than (loosely speaking) the local wave number, which satisfies the local dispersion relation [43]

$$\omega(\boldsymbol{x}, \boldsymbol{k}) = \text{const}. \tag{5}$$

A resonance is a point where $k \to \infty$. (Collisionless dissipation is never negligible at $k \to \infty$, so in reality, a wave always experiences damping near a resonance.) A cutoff is a point where k turns to zero, meaning that a wave experiences reflection. (Definitions of cutoffs can be subtle in multidimensional systems, but that is unimportant for the purposes of this paper.) The area beyond the cutoff, where Eq. (5) has no real solutions for k, is called a forbidden zone. If the forbidden zone is sufficiently narrow, a wave can tunnel through it much like a quantum particle tunnels through a potential barrier.

For X waves, the CMA diagram for the regime that we consider is shown in Fig. 1(a). (There, ω_a is a proxy for ω; the reason why a separate notation ω_a is introduced is explained in Sec. III.) It exhibits the "low-density" cutoff (blue curve) where $\omega_L(x) = \omega$ [42],

$$\omega_L = \frac{1}{2}\left(|\Omega_e| + \sqrt{\Omega_e^2 + 4\omega_p^2}\right), \tag{6}$$

and the UH resonance (red curve) where $\omega_{UH}(x) = \omega$,

$$\omega_{UH} = \sqrt{\Omega_e^2 + \omega_p^2}. \tag{7}$$

The gray area between the cutoff and the resonance is a forbidden zone. This zone narrows at $\omega_p^2/\omega^2 \to 0$ and at $\omega_p^2/\omega^2 \to 1$. Thus, if the wave trajectory enters and exits the forbidden zone in these regions, the entrance and the exit are located close to each other (so a significant amount of the wave energy can tunnel through this zone), forming a pair. There are two such pairs in our case: the low-density cutoff–resonance pair (LCR) and the high-density cutoff–resonance pair (HCR). They will be further discussed in Sec. III, after we explain our choice of the density and magnetic-field profiles, which determine the wave trajectory on the CMA diagram.

III. ONE-DIMENSIONAL MODEL

A. Field configuration

We reduce Eqs. (1) to a one-dimensional system of size $2r_0$. The corresponding space grid $x \in [-r_0/\kappa_x, r_0/\kappa_x]$ has N_x points. For convenience, we define also a space grid s via

$$s = x/\max(x) \tag{8}$$

to have $s \in [-1, 1]$. Because we focus on X-wave propagation, it is enough for us to keep only $\tilde{v}_x, \tilde{v}_y, \tilde{E}_x, \tilde{E}_y$, and $\tilde{B}_z$, and we impose the Dirichlet boundary conditions

$$\tilde{E}_y(-r_0) = \tilde{E}_y(r_0) = 0, \tag{9}$$

$$\tilde{B}_z(-r_0) = \tilde{B}_z(r_0) = 0. \tag{10}$$

To mimic the effect of the antenna that launches the wave, we introduce an auxiliary linear oscillator Q with frequency ω_a (the index a stands for "antenna") and initial amplitude Q_0. Coupled to the magnetic field $\tilde{B}_z$, the oscillator gradually transfers its energy to the X wave, while the energy of the whole system remains constant. Provided that this energy transfer is slow, the wave being launched has an approximately constant frequency, $\omega \approx \omega_a$.

The source is placed at the center ($x = 0$), where the background density (represented by ω_p^2) and magnetic field (represented by Ω_e^2) are small. Thus, the wave trajectory starts at the bottom left corner of the CMA diagram [Fig. 1(a)]. Then the wave propagates both to the left and to the right in the x space. The horizontal black arrow corresponds to the wave propagation toward the HCR. The X wave is partly reflected at the cutoff. But it also partly tunnels through the narrow forbidden zone (gray area) beyond the cutoff (blue line) and accumulates at the UH resonance (red curve), where the wavelength ends up decreasing indefinitely (strictly speaking, until dissipation ceases to be negligible). This is the effect of practical interest that we seek to model, and naturally, doing so requires high resolution near the resonance. However, modeling of this effect can be obscured by wave reflection from the right boundary. To suppress this reflection, auxiliary background profiles are introduced at $x > 0$ [Fig. 1(b)] such that they ensure X-wave trapping inside an additional resonance. Specifically, variations of the density and magnetic field give rise to a LCR and also an additional, *isolated*, UH resonance (IUHR), as shown in Fig. 1(c). Because the LCR is located in the region of extremely small density, the forbidden zone there is practically transparent. Then the wave energy propagating from the source to the right ($x > 0$) goes through the LCR without noticeable reflection and accumulates at the IUHR, so no reflection from the right boundary ever occurs. Classical simulations of this system [Figs. 2(a) and 2(b)] show that the wave behaves as described indeed.

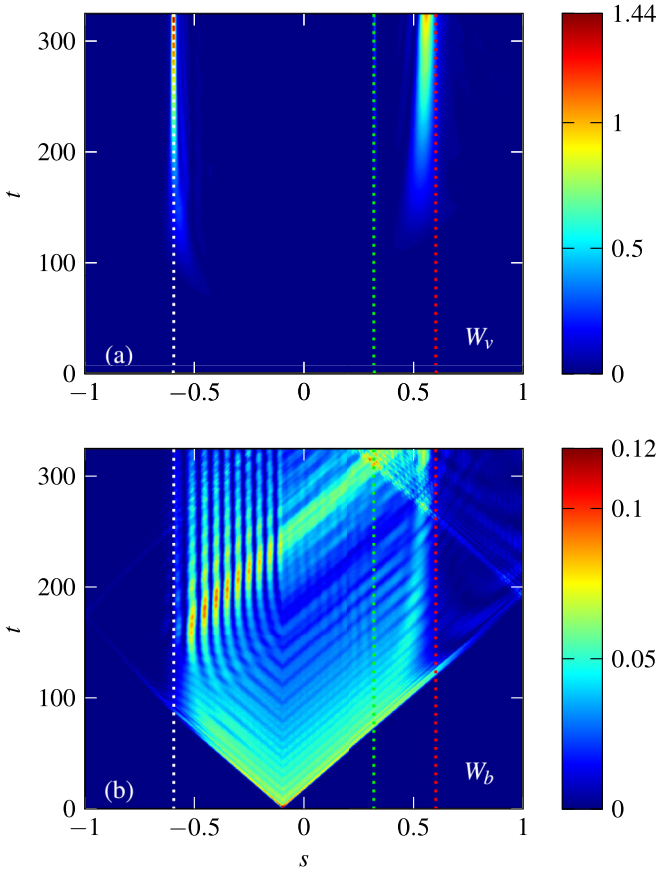

FIG. 2. Classical simulation: Dynamics of kinetic energy W_v (a) and magnetic energy W_b (b) in space and time. The input parameters are described in Sec. VI. The white line indicates the HCR; the red line indicates the IUHR; the green line indicates the LCR [Fig. 1(a)]. The left-propagating wave reaches the HCR, partially reflects from it, and partially tunnels to the UH resonance. The right-propagating wave is trapped within the IUHR, and only a small part of its energy reaches the right boundary.

B. Rescaled variables

In terms of the rescaled velocity $\xi = \tilde{v}\sqrt{n}$, our one-dimensional model can be written explicitly as

$$i\partial_t \xi_x(x,t) = -iB_0(x)\xi_y(x,t) - i\sqrt{n(x)}\tilde{E}_x(x,t), \quad (11a)$$

$$i\partial_t \xi_y(x,t) = iB_0(x)\xi_x(x,t) - i\sqrt{n(x)}\tilde{E}_y(x,t), \quad (11b)$$

$$i\partial_t \tilde{E}_x(x,t) = i\sqrt{n(x)}\xi_x(x,t), \quad (11c)$$

$$i\partial_t \tilde{E}_y(x,t) = i\sqrt{n(x)}\xi_y(x,t) - i\partial_x \tilde{B}_z(x,t), \quad (11d)$$

$$i\partial_t \tilde{B}_z(x \neq x_q,t) = -i\partial_x \tilde{E}_y(x \neq x_q,t), \quad (11e)$$

$$i\partial_t \tilde{B}_z(x_q,t) = -i\partial_x \tilde{E}_y(x_q,t) - \beta Q(x_q,t), \quad (11f)$$

$$i\partial_t Q(x_q,t) = -\omega_a Q(x_q,t) - \beta \tilde{B}_z(x_q,t), \quad (11g)$$

$$Q(x_{q_1},0) = Q(x_{q_2},0) = Q_0, \quad (11h)$$

where the source Q with a constant frequency ω_a is coupled to the magnetic field $\tilde{B}_z$ using an *ad hoc* coupling coefficient β. The 1-D model can be rewritten in the Hamiltonian form [Eq. (3)] with

$$\psi = (\xi_x, \xi_y, \tilde{E}_x, \tilde{E}_y, \tilde{B}_z, Q)^\intercal, \quad (12)$$

where $^\intercal$ denotes transposition. The energy density $W_{\text{tot}} = \psi\psi^\dagger$ is then represented as $W_{\text{tot}} = W_v + W_{eb} + W_q$, where

$$W_v = |\xi_x|^2 + |\xi_y|^2, \quad (13a)$$

$$W_{eb} = |\tilde{E}_x|^2 + |\tilde{E}_y|^2 + |\tilde{B}_z|^2, \quad (13b)$$

$$W_q = |Q|^2. \quad (13c)$$

C. Discretization

The x axis is represented by $N_x = 2^{n_x}$ points with a step h (Fig. 3). Equations (11) are discretized in space using the

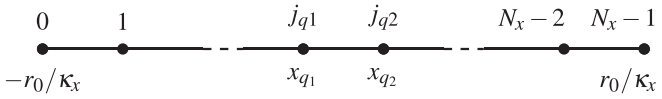

FIG. 3. One-dimensional space grid $x \in [-r_0/\kappa_x, r_0/\kappa_x]$ has N_x points numerated by index j, starting with $j = 0$. The source Q is placed at points x_{q_1} and x_{q_2} that correspond to the indices j_{q_1} and j_{q_2}.

central differencing scheme. The boundary conditions for the velocity are

$$i\partial\xi_{y,0} = iB_{0,0}\xi_{x,0}, \tag{14a}$$

$$i\partial\xi_{y,N_x-1} = iB_{0,N_x-1}\xi_{x,N_x-1}, \tag{14b}$$

for the wave electric field they are

$$i\partial_t\tilde{E}_{y,0} = 0, \tag{15a}$$

$$i\partial_t\tilde{E}_{y,1} = i\sqrt{n_1}\xi_{y,1} - \frac{i}{2h}\tilde{B}_{z,2}, \tag{15b}$$

$$i\partial_t\tilde{E}_{y,N_x-2} = i\sqrt{n_{N_x-2}}\xi_{y,N_x-2} + \frac{i}{2h}\tilde{B}_{z,N_x-3}, \tag{15c}$$

$$i\partial_t\tilde{E}_{y,N_x-1} = 0, \tag{15d}$$

and for the magnetic field they are

$$i\partial_t\tilde{B}_{z,0} = 0, \tag{16a}$$

$$i\partial_t\tilde{B}_{z,1} = -\frac{i}{2h}\tilde{E}_{y,2}, \tag{16b}$$

$$i\partial_t\tilde{B}_{z,N_x-2} = \frac{i}{2h}\tilde{E}_{y,N_x-3}, \tag{16c}$$

$$i\partial_t\tilde{B}_{z,N_x-1} = 0. \tag{16d}$$

Since the source Q interacts with the wave magnetic field only at the center of the system [Eqs. (11f)–(11g); Fig. 3], it does not enter the boundary conditions. The corresponding Hamiltonian can be expressed as

$$\mathscr{H} = \begin{pmatrix} 0 & -iB_0 & -i\sqrt{n} & 0 & 0 & 0 \\ iB_0 & 0 & 0 & -i\sqrt{n}\varepsilon & 0 & 0 \\ i\sqrt{n} & 0 & 0 & 0 & 0 & 0 \\ 0 & i\sqrt{n}\varepsilon & 0 & 0 & M_h & 0 \\ 0 & 0 & 0 & M_h & 0 & M_\beta \\ 0 & 0 & 0 & 0 & M_\beta & M_{\omega_a} \end{pmatrix}. \tag{17}$$

Here, $\varepsilon = \mathrm{diag}(0, 1, \ldots, 1, 0)$, and M_h is the matrix representation of the operator ∂_x:

$$M_h = \begin{pmatrix} 0 & 0 & 0 & 0 & \ldots \\ 0 & 0 & -\frac{i}{2h} & 0 & \ldots \\ 0 & \frac{i}{2h} & 0 & -\frac{i}{2h} & \ldots \\ \ldots & \ldots & \ldots & \ldots & \ldots \\ \ldots & \frac{i}{2h} & 0 & -\frac{i}{2h} & 0 \\ \ldots & 0 & \frac{i}{2h} & 0 & 0 \\ \ldots & 0 & 0 & 0 & 0 \end{pmatrix}. \tag{18}$$

The matrix M_β describes the source-wave coupling,

$$M_\beta = \begin{pmatrix} \ldots & \ldots & \ldots & \ldots & \ldots & \ldots \\ \ldots & 0 & 0 & 0 & 0 & \ldots \\ \ldots & 0 & -\beta & 0 & 0 & \ldots \\ \ldots & 0 & 0 & -\beta & 0 & \ldots \\ \ldots & 0 & 0 & 0 & 0 & \ldots \\ \ldots & \ldots & \ldots & \ldots & \ldots & \ldots \end{pmatrix}, \tag{19}$$

while M_{ω_a} encodes the source frequency,

$$M_{\omega_a} = \begin{pmatrix} \ldots & \ldots & \ldots & \ldots & \ldots & \ldots \\ \ldots & 0 & 0 & 0 & 0 & \ldots \\ \ldots & 0 & -\omega_a & 0 & 0 & \ldots \\ \ldots & 0 & 0 & -\omega_a & 0 & \ldots \\ \ldots & 0 & 0 & 0 & 0 & \ldots \\ \ldots & \ldots & \ldots & \ldots & \ldots & \ldots \end{pmatrix}. \tag{20}$$

Here, B_0 is a diagonal $N_x \times N_x$ matrix with values of the background magnetic field on the diagonal. The matrix that encodes $\sqrt{n(x)}$ has the same form. The coefficients β and ω_a are placed at the diagonal elements (j_{q_1}, j_{q_1}) and (j_{q_2}, j_{q_2}) of the matrices M_β and M_{ω_a}. Finally, the values $i/2h$ are shifted by $+1$ and -1 with respect to the diagonal of the matrix M_h.

D. Quantum encoding of plasma signals

To encode our discretized system into a quantum circuit, we map ψ on two registers: $|d\rangle$ and $|j\rangle$. The register $|j\rangle$ has $n_x = \log_2 N_x$ qubits and stores the space dependence of every variable. That is, $|j\rangle$ contains the binary representation of the spatial-point indices in the x grid. The register $|d\rangle$ encodes the variable index:

$$d = 0 \longleftrightarrow \xi_x, \tag{21a}$$

$$d = 1 \longleftrightarrow \xi_y, \tag{21b}$$

$$d = 2 \longleftrightarrow \tilde{E}_x, \tag{21c}$$

etc. Since we have six independent fields in ψ, the register $|d\rangle$ must have at least three qubits. Then,

$$\psi = A_{d,j}|d\rangle|j\rangle \equiv A_{d,j}|d_2 d_1 d_0\rangle_d|j_{n_x-1}\ldots j_2 j_1 j_0\rangle_j, \tag{22}$$

where d_k and j_k take values of 0 or 1; $A_{d,j}$ stores the amplitude of the variable with the index d at x_j. For instance, the value of $\tilde{B}_z(x = x_5)$ is stored in $A_{d=4,j=5}$, which is the amplitude of the quantum state $|100\rangle_d|0\ldots0101\rangle_j$. We assume that the rightmost qubit is the least-significant one (i.e. the one that determines parity), which is the bottom qubit in the quantum circuit.

E. Initialization

The source Q is initialized at two spatial points with indices j_q and $(j_q + 1)$ such that j_q is even and close to $N_x/2$, i.e., at the center of the system. There, the plasma density is low, so the X-wave wave number is $k_x = \omega_a/c$. To guarantee the state normalization $\langle\psi|\psi\rangle = 1.0$, we set $Q_0 = 1/\sqrt{2}$ [Eq. (11h)]. To prepare this initial state, one sets $|0\rangle_j$ and $|5\rangle_d$. Then, a Hadamard gate is placed at the least-significant qubit of the register $|j\rangle$. Apart from that, every qubit that must have a value 1 according to the bit representation of the integer j_q is inverted by a Pauli X gate. An example of the initialization circuit for $n_x = 4$ is shown in Fig. 4. The proper initialization is confirmed by the comparison of the source time evolution from classical and QC modeling shown in Figs. 17(a) and 17(c). If one wants to initialize a source with various amplitudes at different spatial points, one can use one or several rotation gates R_y [Eq. (36)] instead of the Hadamard gate. The

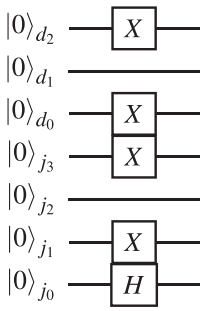

FIG. 4. An example of the quantum-state initialization in a system with $n_x = 4$, where the source Q, which is stored in $|5\rangle_d \equiv |101\rangle_d$, is placed at x points with $j_q = 10$ and 11.

number of gates in the initialization circuit is proportional to n_x.

IV. QUANTUM-SIGNAL-PROCESSING FRAMEWORK

A. QSP basics

Quantum signal processing (QSP) [33,34,44] is an algorithm for constructing a polynomial $f(A)$ of a given matrix A. In the case of Hamiltonian simulations, QSP is used for approximating the propagator with a given absolute error, as $f(\mathscr{H}) \approx \exp(-i\mathscr{H}t) + \mathscr{O}(\varepsilon_{\rm qsp})$, and encodes the polynomial into a quantum circuit as

$$U_{\rm qsp} = \begin{pmatrix} f(\mathscr{H}) & \cdot \\ \cdot & \cdot \end{pmatrix}. \tag{23}$$

Here, the unitary matrix $U_{\rm qsp}$ depends on $(2N_\phi + 1)$ real parameters ϕ_j, henceforth called *phases*, and is represented by a set of rotations [33,36] (Fig. 5):

$$U_{\rm qsp} = R_{z,b}(\phi_{2N_\phi})\, \Phi_{N_\phi - 1}(\phi_{2N_\phi - 1}, \phi_{2N_\phi - 2}) \ldots \Phi_0(\phi_1, \phi_0). \tag{24}$$

Unlike in graphical representations of quantum circuits, the rightmost operator Φ_0 is applied first, and the leftmost operator $R_{z,b}$ is applied last. The latter is the Pauli rotation gate:

$$R_z(\phi) = \begin{pmatrix} \exp(-i\phi/2) & 0 \\ 0 & \exp(i\phi/2) \end{pmatrix}, \tag{25}$$

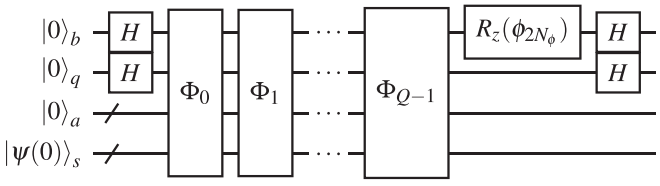

FIG. 5. General QSP circuit [Eq. (24)]. The subcircuit for each $\Phi_j(\phi_{2j+1}, \phi_{2j})$ is shown in Fig. 6. The rotation gate R_z is defined in Eq. (25). The ancillae $|a\rangle, |q\rangle, |b\rangle$ are initialized in the zero state, while the register $|s\rangle$ stores the initial conditions. The Hadamard gates H prepare the necessary superposition state $|+\rangle$ for the ancillae $|q\rangle$ and $|b\rangle$. If all ancillae are output in the zero state, then the register $|s\rangle$ contains the QSP approximation of $\exp(-i\mathscr{H}t)|\psi(0)\rangle_s$ for the given t and error $\varepsilon_{\rm qsp}$.

which acts on the ancilla qubit $|b\rangle$. The operator $\Phi_j(\phi_{2j+1}, \phi_{2j})$ is described in Fig. 6. It consists of alternating rotation gates R_z [Eq. (25)] and an operator W [Eq. (33)], which encodes the Hamiltonian (Sec. IV C). The copies of W create higher powers of $\mathscr{H}$, which are used to construct the polynomial $f(\mathscr{H})$, while the rotations R_z generate the appropriate coefficients in $f(\mathscr{H})$ [33,34].

An initial state $\psi(0)$ is stored in the input register $|s\rangle$ (in our case, the combination of registers $|d\rangle$ and $|j\rangle$), and the ancillae $|b\rangle$, $|q\rangle$, and $|a\rangle$ are initialized in the zero state. Then, QHS is implemented via application of the unitary $U_{\rm qsp}$ to the system state vector. Because the propagator is encoded as the upper-left block of $U_{\rm qsp}$, the desired state $\exp(-i\mathscr{H}t)\psi(0)$ is yielded as the output in the register $|s\rangle$ when all the ancillae are measured in the zero state. In Hamiltonian simulations by the QSP method, the probability of the postselected state is close to unity, $1 - \varepsilon$, with an arbitrary small ε, which is determined by the QSP approximation error [45].

The phases are chosen depending on the simulation time and error tolerance $\varepsilon_{\rm qsp}$, and are calculated on a classical computer using known algorithms. The corresponding details can be found in Refs. [36–38]. The codes for the calculation of the phases are presented in Refs. [46,47]. In our work, we use the code described in Ref. [36] and presented in Ref. [46].

B. Block encoding

The operator W (Fig. 7) contains an oracle U_H that is the mapping of the Hamiltonian $\mathscr{H}$ on a unitary matrix. In this work, circuit representation of any function or mapping is called an oracle. Generally, a Hamiltonian is a nonunitary matrix; it cannot be directly described by a quantum circuit, which can contain only unitary gates. Therefore, to operate with $\mathscr{H}$ in the QSP circuit, one has to encode $\mathscr{H}$ within a unitary matrix. The corresponding mapping $\mathscr{H} \to U_H$ is called block encoding. This transformation can be done by extending Hilbert space such that the matrix $\mathscr{H}$ becomes a subblock of the unitary U_H:

$$U_H = \begin{pmatrix} \frac{\mathscr{H}}{\varsigma M} & \cdot \\ \cdot & \cdot \end{pmatrix}, \tag{26}$$

where the original matrix $\mathscr{H}$ must be normalized to its norm

$$M \equiv ||\mathscr{H}||_{\rm max} = \max_i \sum_j \sqrt{|\mathscr{H}_{ij}|^2}, \tag{27}$$

and to its sparsity ς (the number of nonzero elements in a row or a column maximized over all rows and columns). The extension of the space is achieved by using the ancilla register $|a\rangle$. The block encoding as shown in Eq. (26) indicates that the normalized Hamiltonian can be extracted from U_H when the ancillae have zero input and output states:

$$\langle k|_s \langle 0|_a U_H |0\rangle_a |j\rangle_s = \frac{\mathscr{H}_{jk}}{\varsigma M}. \tag{28}$$

Here, the row index j is encoded as an input in the register $|s\rangle$, and the column index k is an output in the same register after the block-encoding operation. This can be understood as a decomposition of the Hamiltonian into a collection of its nonzero elements, $\mathscr{H} = \sum \mathscr{H}_{jk}|k\rangle\langle j|$, which is optimal for sparse $\mathscr{H}$. Efficiency of the QSP technique is usually

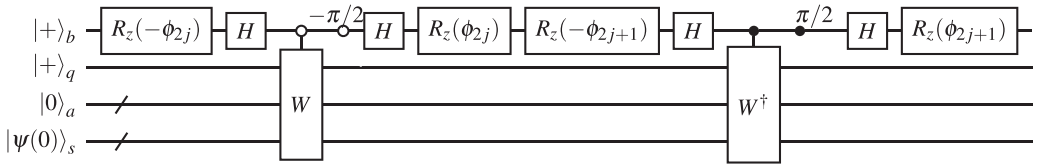

FIG. 6. Quantum circuit of each operator $\Phi_j(\phi_{2j+1}, \phi_{2j})$ that enters Eq. (24).

estimated in a number of queries to the oracle U_H. The block encoding of our wave Hamiltonian [Eq. (17)] is discussed in Sec. V.

C. Qubitization

The purpose of the QSP is to build the desired polynomial $f(\mathscr{H})$. Because U_H is linear in $\mathscr{H}$, multiple applications of U_H are required, where the block-encoding matrix acts as

$$U_H|0\rangle_a|\lambda\rangle_s = \lambda|0\rangle_a|\lambda\rangle_s + \sqrt{1-\lambda^2}|\perp\rangle_{a,s}. \tag{29}$$

Here, $\lambda, |\lambda\rangle$ are the eigenvalue and eigenvector of $\mathscr{H}$, respectively; the state $|\perp\rangle_{a,s}$ is created by the undefined part of U_H marked with dots in Eq. (26). To build higher powers of $\mathscr{H}$, we need to stay within the space spanned by $(|0\rangle_a|\lambda\rangle_s, U_H|0\rangle_a|\lambda\rangle_s)$. The problem is that in general, this space is not invariant under the action of U_H. Every next application of U_H adds additional perpendicular vectors that are different from the original $|\perp\rangle_{a,s}$. To overcome this issue, one can decompose ("qubitize") [34] the entire Hilbert space into two-dimensional orthogonal subspaces, $\bigoplus_\lambda \mathscr{P}_\lambda$, where each subspace $\mathscr{P}_\lambda$ corresponds to a particular $|\lambda\rangle$ of $\mathscr{H}$. After that, one replaces U_H by a new operator W that performs rotation in each of these disjoint subspaces. As a result, the operator W block-encodes $\mathscr{H}$ and, by acting in an invariant space $\mathscr{P}_\lambda = (|0\rangle_a|\lambda\rangle_s, W|0\rangle_a|\lambda\rangle_s)$ for each $|\lambda\rangle$, can produce the necessary moments of $\mathscr{H}$ to construct the polynomial $f(\mathscr{H})$.

According to Lemma 10 from Ref. [34], W can always be constructed using the following procedure. First of all, one again extends the Hilbert space with an ancilla $|q\rangle$ initialized in the superposition state $|+\rangle = (|0\rangle + |1\rangle)/\sqrt{2}$:

$$|0\rangle_a \to |+\rangle_q|0\rangle_a. \tag{30}$$

Then, one applies an X gate to the ancilla $|q\rangle$,

$$S = X_q \otimes I_{a,s}, \tag{31}$$

and uses two copies of controlled U_H,

$$U_H' = |0\rangle_q\langle 0|_q \otimes U_H + |1\rangle_q\langle 1|_q \otimes U_H^\dagger. \tag{32}$$

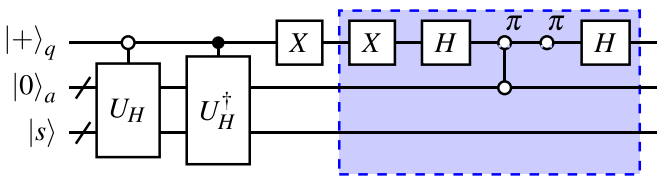

FIG. 7. Quantum circuit of the operator W [Eq. (33)]. The controlled unitary U_H [Eq. (26)] and its complex conjugate $U_H^\dagger$ form the extended operator U_H' [Eq. (32)]. The left Pauli X gate implements the operator S [Eq. (31)]. The subcircuit within the blue box implements the reflector U_R [Eq. (34)].

Combining the above operators, one constructs

$$W = (U_R \otimes I_s)SU_H', \tag{33}$$

where the so-called reflector U_R,

$$U_R = 2|+\rangle_q|0\rangle_a\langle 0|_a\langle +|_q - I_{q,a}, \tag{34}$$

keeps unchanged the zero-ancilla state and inverts the sign of the perpendicular state. Here, I_y is the unit operator that acts on a given ancilla $|y\rangle$. The corresponding circuit is shown in Fig. 7. As is proven in Lemma 8 and Lemma 10 from Ref. [34], the above construction guarantees that the matrix form of the operator W is represented by the following direct sum,

$$W = \bigoplus_\lambda \begin{pmatrix} \lambda & -\sqrt{1-\lambda^2} \\ \sqrt{1-\lambda^2} & \lambda \end{pmatrix}, \tag{35}$$

which ensures the invariance of each subspace $\mathscr{P}_\lambda$ under the action of W.

V. BLOCK ENCODING OF THE WAVE HAMILTONIAN

A. General algorithm

To encode the wave Hamiltonian [Eq. (17)], we apply the state-preparation technique [34]. The standard procedure is described in Appendix A. In this algorithm, one finds positions of all nonzero elements within $\mathscr{H}$ and then encodes values of these elements into the amplitudes of quantum states. First of all, for each row of $\mathscr{H}$ one stores the column indices of nonzero matrix elements in an ancilla register. Being an integer, each index is encoded as a quantum state represented by a bit string of qubits. After that, knowing the column and row indices, one finds the values of the corresponding nonzero elements. The values are encoded in the amplitudes of the quantum states. Since any element of the rescaled Hamiltonian $\mathscr{H}/(\varsigma M)$ [Eq. (26)] is less than (or equal to) unity by the absolute value, it can be represented as $\cos(\theta/2)$ of a certain angle θ. The cosine can be generated by the rotation gate $R_y(\theta)$,

$$R_y(\theta) = \begin{pmatrix} \cos(\theta/2) & -\sin(\theta/2) \\ \sin(\theta/2) & \cos(\theta/2) \end{pmatrix}, \tag{36}$$

acting on the zero state,

$$R_y(\theta)|0\rangle = \cos(\theta/2)|0\rangle + \sin(\theta/2)|1\rangle. \tag{37}$$

B. Normalization

To normalize the wave Hamiltonian [Eq. (17)], we adopt

$$\mathscr{H}_{\rm qsp} = \beta_H \mathscr{H}, \quad t_{\rm qsp} = t/\beta_H, \quad \beta_H = \frac{1}{d_H^2 M}, \tag{38}$$

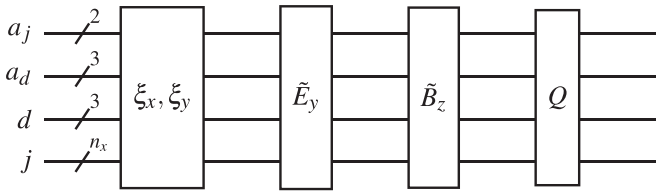

FIG. 8. General circuit of the oracle O_F. Its components are shown in Fig. 9. According to Table I, the block $\tilde{E}_x$ does not modify ancillae $|a_j\rangle|a_d\rangle$.

or more explicitly,

$$\beta_H = \frac{1}{d_H^2\sqrt{\omega_{\mathrm{UH,max}}^2 + \frac{1}{2h^2} + \beta^2 + \omega_a^2}}. \tag{39}$$

Here, $\mathscr{H}_{\mathrm{qsp}}$ is the rescaled Hamiltonian, t_{qsp} is the time interval to be simulated by the QSP circuit, $\omega_{\mathrm{UH,max}} = \sqrt{B_{0,\mathrm{max}}^2 + n_{\mathrm{max}}}$, and n_{max} and $B_{0,\mathrm{max}}$ are the maximum values of the background density and magnetic field, respectively. In our case, $d_H^2 = 4$, which is related to the sparsity ς in Eq. (28) as is explained in Appendix B.

Note that larger t_{qsp} requires calculation of a higher number of QSP phases, which can be challenging. Instead of doing that, we represent the QSP circuit with n_t sequential copies of a shorter circuit constructed for the time interval t_{qsp}/n_t. In this case, performing simulations on a digital emulator, one can also analyze intermediate quantum states.

C. Ancilla registers

To implement the state-preparation method (Appendix A), we introduce several ancilla registers (Fig. 8) to store positions of matrix nonzero elements. The register $|a_d\rangle$ is responsible for the location of subblocks such as M_h or M_β in Eq. (17). Given a variable index $|d\rangle$ [Eq. (22)], the register $|a_d\rangle$ stores the absolute column indices of all subblocks that contain nonzero elements. The maximum number of subblocks in a row (including zero subblocks) coincides with the number of variables in our plasma system. Thus, the size of $|a_d\rangle$ is the same as that of the register $|d\rangle$.

Then, we describe the location of nonzero elements within each subblock. The ancilla register $|a_j\rangle$ is introduced for this purpose. To decrease the total number of ancillae, this register stores not an absolute column index but the relative position of a nonzero element with respect to the subblock diagonal,

$$|00\rangle_{a_j} \to i_c = i_r, \tag{40}$$

$$|01\rangle_{a_j} \to i_c = i_r - 1, \tag{41}$$

$$|10\rangle_{a_j} \to i_c = i_r + 1, \tag{42}$$

where i_r is the row index, which is the index of a given point on the x grid of a variable. The row index is stored in the register $|j\rangle$ [Eq. (22)]. The integer i_c is the column index of the nonzero value within the subblock $|a_d\rangle$. For instance, $|00\rangle_{a_j}$ means that a nonzero element lies on the local diagonal of the subblock. One should note that the size of the register $|a_j\rangle$ does not depend on N_x, which is not the case in the standard technique (Appendix A). This feature allows us to increase N_x without increasing the number of ancillae. The size of $|a_j\rangle$ increases, however, with the discretization order and it may also depend on the boundary conditions.

Finally, two more single-qubit ancilla registers $|a_1\rangle$ and $|a_2\rangle$ are introduced. The rotation gates $R_y(\theta)$ act on these qubits to store the nonzero elements of the Hamiltonian [Eq. (37)]. A thinner space grid has a smaller difference between neighboring Hamiltonian elements, and as a result, requires that the rotation angle θ be calculated with a higher precision.

D. Block-encoding operator

Now, when we have introduced all necessary ancillae and know how they store the structure of $\mathscr{H}$, we can represent the block encoding as a product of several operators,

$$U_H = O_F^\dagger O_{\sqrt{H},a_2}^\dagger O_M O_{S,a_1} O_{\sqrt{H},a_1} O_F, \tag{43}$$

where every operator is responsible for a particular part of the block-encoding procedure. The oracle O_F (Table I; Figs. 8–9 and Fig. 10) defines the location of nonzero elements for a given variable index stored in $|d\rangle$ and for a local row index saved in $|j\rangle$. This oracle writes the column indices of subblocks with nonzero elements into the register $|a_d\rangle$ and local relative positions of these nonzero elements into the register $|a_j\rangle$. To construct the quantum circuit of the oracle O_F, we consider it as a sequence of subcircuits for different variables (Fig. 8). Every subcircuit corresponds to one block from Table I. If one assumes that multicontrolled gates are physically realizable, then the depth of the O_F circuit does not change with the system size N_x. However, whether it will be possible to efficiently connect non-neighboring qubits in future quantum computers is yet to be seen. Transpiling the multicontrolled gates into one-qubit and two-qubit gates using a nonoptimized algorithm makes the circuit depth grow exponentially with the number of qubits. However, as shown in Ref. [48], by using a sufficient number of ancillae one can decompose an arbitrary n_q-controlled unitary matrix into $\mathscr{O}(n_q^2)$ elementary gates. For instance, an n_q-controlled Pauli X gate can be transpiled into $4(n_q - 2)$ 2-controlled X gates (so-called Toffoli gates) by adding $n_q - 2$ ancilla qubits.

The oracle $O_{\sqrt{H}}$ (Table II; Fig. 11) reads the row and column indices and provides the square root of the absolute value of the corresponding nonzero element. It acts on the ancilla $|a_1\rangle$ or ancilla $|a_2\rangle$. The oracle O_{S,a_1} (Table III; Fig. 12) describes whether an element is imaginary or real, as well as whether it is positive or negative.

In the standard state-preparation algorithm, ancilla registers store the absolute column indices [Eqs. (A4) and (A5)]. As a result, the index exchange between the ancilla and input registers can be implemented by a simple swap operator. In our case, the register $|a_j\rangle$ works with relative indices. Because of that, we need to implement the mapping between the absolute and relative indices during the index exchange. This is provided by the oracle O_M (Fig. 13) by using a subtractor and an adder by 1, which are depicted in Fig. 14. After the application of the oracle O_M, the register $|j\rangle$ encodes the absolute column indices of nonzero elements within a subblock, and the register $|d\rangle$ contains subblock column indices. The depth

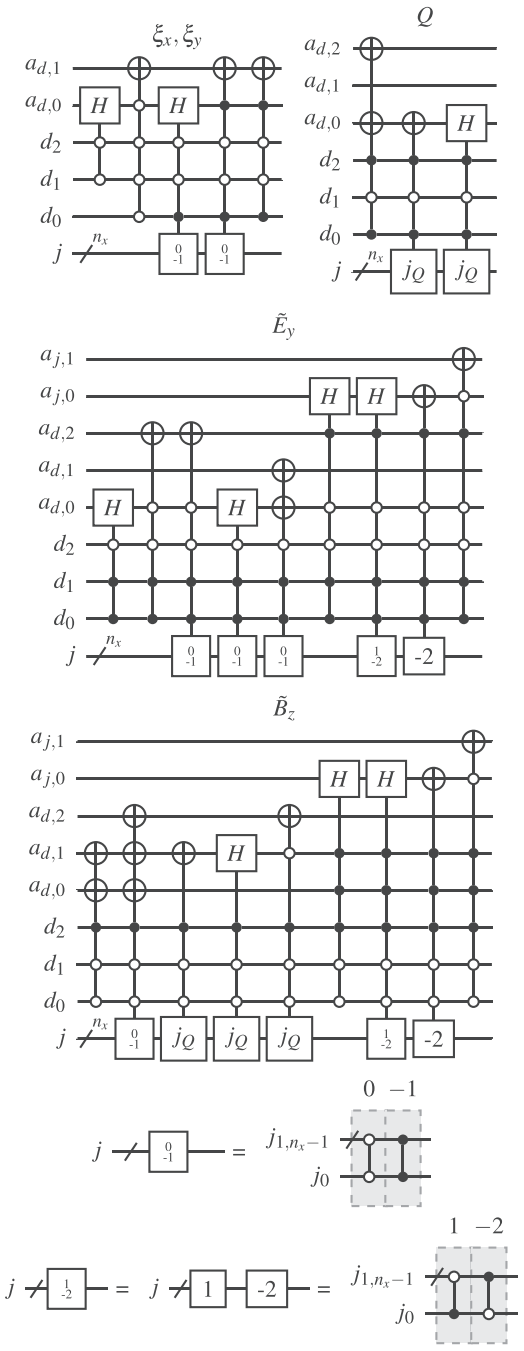

FIG. 9. Subblocks of the O_F quantum circuit shown in Fig. 8. The circuits are constructed following Table I. The control block j_Q is illustrated in Fig. 10. The control nodes in the register $|d\rangle$ encode the variable label, while the register $|j\rangle$ encodes the spatial coordinate.

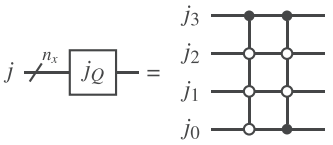

FIG. 10. Circuit of the control block j_Q in a system with $n_x = 4$, where the source Q is placed at spatial points with indices $j_{q,1} = 8$ and $j_{q,2} = 9$.

of the circuit O_M is proportional to $\log_2(N_x)$ because of the adder and subtractor.

To sum up, taking the row index as an input in $|d\rangle|j\rangle$ and the ancillae initialized in the zero state, the resulting oracle U_H outputs column indices encoded in $|d\rangle|j\rangle$ as states with amplitudes equal to the corresponding Hamiltonian elements when all ancillae registers are returned in the zero state [Eq. (28)].

VI. SIMULATION RESULTS

A. Comparison of classical and quantum simulations

We implement QHS using the circuit described above on a classical emulator of a quantum computer using the QuEST toolkit [41]. The code and the corresponding input data for the simulations can be found in Ref. [49]. Unlike in an actual quantum simulation, this gives us access to the whole output space at all moments of time. The results presented below are directly extracted from ψ [Eq. (22)] without performing, or emulating, quantum measurements. Then, we compare our results with those of classical simulations, which have been obtained by directly solving Eqs. (11) using the central finite difference scheme for both space and time. As a reminder, the normalized background profiles are shown in Fig. 1(b). The size of the system is $r_0 = 20$ cm with $N_x = 1024$ spatial points, which corresponds to $n_x = 10$. The simulation time is $t_f = 300.5\omega_p^{-1}$, which is split into $n_t = 1200$ time steps with duration $\tau = 0.2504\omega_p^{-1}$. The corresponding Courant number is 0.76.

The background density and magnetic field profiles are calculated by the following equations (here $r = x\kappa_x$):

$$n(r) = n_0 e^{-\frac{(r-r_n)^2}{2\Delta_n^2}} + n_{0,\mathrm{aux}} e^{-\frac{(r-r_{n,\mathrm{aux}})^2}{2\Delta_{n,\mathrm{aux}}^2}}, \tag{44a}$$

$$B_0(r) = \begin{cases} \frac{B_c R_0}{R_0 + r}, & r < r_{\mathrm{aux}}, \\ \frac{B_{c,\mathrm{aux}} R_{0,\mathrm{aux}}}{R_{0,\mathrm{aux}} + (r - r_{\mathrm{aux}})}, & r \geqslant r_{\mathrm{aux}}. \end{cases} \tag{44b}$$

The maximum background density is $n_0 = 2 \times 10^{13}$ cm^{-3} at $r_n = -0.99 r_0$, while the peak of the auxiliary density profile is $n_{0,\mathrm{aux}} = 10^{12}$ cm^{-3} at $r_{n,\mathrm{aux}} = 0.90 r_0$. The widths of the density peaks are $\Delta_n = 0.2 r_0$ and $\Delta_{n,\mathrm{aux}} = 0.18 r_0$, correspondingly. The background magnetic field at the center ($r = 0$) is $B_c = 1$ kG, and the auxiliary magnetic peak at $s = 0.4$ ($r_{\mathrm{aux}} = 0.4 r_0$) has $B_{c,\mathrm{aux}} = 7$ kG. The shape of the field is defined by two parameters: the major radius $R_0 = 167$ cm and the auxiliary radius $R_{0,\mathrm{aux}} = 10$ cm. The profiles of the background magnetic field are combined by the cubic interpolation in a narrow domain near $r = r_{\mathrm{aux}}$. The source-field coupling coefficient is $\beta = 0.1$, and Q oscillates with the frequency $\omega_a = 0.38\omega_{p,0}$. The corresponding wave number is $k_x = 64.56 r_0^{-1}$. With these parameters, the normalization of the Hamiltonian [Eq. (39)] becomes $\beta_H = 0.102$. Therefore, the QSP time step is $\tau_{\mathrm{qsp}} = \tau/\beta_H = 2.455$ with the resulting time interval $t_{\mathrm{qsp}} = n_t \tau_{\mathrm{qsp}} = 2946$ to simulate. The QSP error is $\varepsilon_{\mathrm{qsp}} = 10^{-6}$. As seen from Fig. 15(a), such $\varepsilon_{\mathrm{qsp}}$ corresponds to $\sim 10^{-4}$ error in the energy conservation. For this QSP error, the number of QSP angles is equal to 25 for the time interval τ_{qsp}.

According to Ref. [34], the query complexity (the number of copies of the oracle U_H) of the QSP circuit is $\mathcal{O}(t_{\mathrm{qsp}} + \log_2(1/\varepsilon_{\mathrm{qsp}}))$. The asymptotic dependence is confirmed by

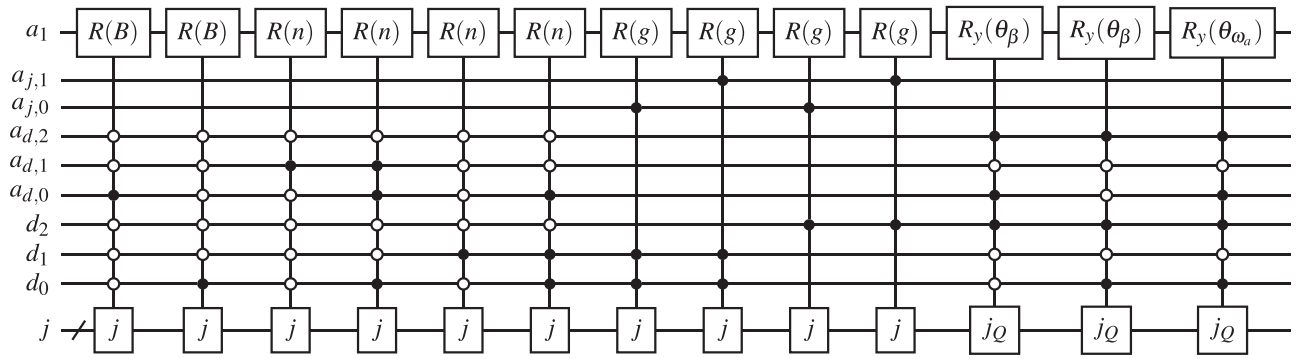

FIG. 11. Quantum circuit of the oracle $O_{\sqrt{H},a_1}$. Every box j indicates the conditional dependence on the register $|j\rangle$. Here, the conditional-rotation gate $R(B)$ is used to obtain the profile $\sqrt{\beta_H B_{0,j}}$; $R(n)$ encodes the profile $\sqrt{\beta_H n_j^{1/2}}$; $R(g)$ encodes a constant $\sqrt{\beta_H/(2h)}$ with different superpositions for bulk and boundary x points. In our model, the conditional-rotation gates are represented by multiqubit matrices. The circuit is built according to Table II.

our direct computation [Figs. 16(a) and 16(b)]. There, the total number of queries is calculated as twice the number of the QSP phases, because each phase corresponds to two calls to the block-encoding oracle U_H (Figs. 6 and 7). The number of the phases is found using the code from Ref. [46]. In our particular case, where the whole QSP circuit is split into n_t subcircuits, the query complexity scales as $\mathcal{O}(n_t \tau_{\rm qsp} + n_t \log_2(1/\varepsilon_{\rm qsp}))$.

We compare the time evolution of the energy components [Eqs. (13a)–(13c)] integrated in space. Figure 15(b) shows that both the classical and quantum simulations produce the same time histories of various energy components [Eqs. (13a)–(13c)]. When the wave reaches the HCR [at $t \approx 100$, according to Fig. 2(b)], the field energy converts partly into the kinetic plasma energy. Figures 17(b), 17(d) show that the kinetic (field) energy has a similar spatial distribution in both the simulations, and the X wave accumulates in the UH resonance of the HCR. The wave also passes the LCR practically without interaction and deposits its energy at the IUHR, as anticipated.

B. Oracle scaling

Assuming that multiqubit controlled gates are realizable, the depths of the oracles O_F (Fig. 8) and O_S (Fig. 12) are independent of $n_x = \log_2 N_x$. However, these depths can change if the discretization order is increased or if the source Q is distributed over multiple grid points. The depth of the oracle O_M increases linearly with n_x due to the adder and subtractor (Fig. 14).

The oracle $O_{\sqrt{H}}$ (Fig. 11) depends on n_x due to the conditional-rotation gates, as is discussed in Appendix B. Similar gates are considered in Ref. [39] (see supplemental materials there), where they are called multiplexed unitaries. These gates can be implemented via arithmetic functions that usually scale as $\mathcal{O}(\text{poly}(n_x))$. For instance, as shown in Ref. [1], the depth of a general adder with one of the summands predefined scales as $\mathcal{O}(n_x)$, and the subtractor depth scales as $\mathcal{O}(n_x) + 2n_x$. In general, there is a trade between the number of ancillae used to store intermediate data and the depth of the resulting circuit. In our case, a conditional-rotation gate must implement a smooth function that depends on the space variable x encoded inside the register $|j\rangle$. As explained in Ref. [50], a polynomial of order D can be evaluated by using the Horner scheme. A given polynomial y_D with coefficients a_i can be obtained by D subsequent iterations:

$$
\begin{aligned}
y_1 &= a_D x + a_{D-1}, \\
y_2 &= y_1 x + a_{D-2}, \\
&\cdots \\
y_D &= y_{D-1} x + a_0.
\end{aligned}
$$

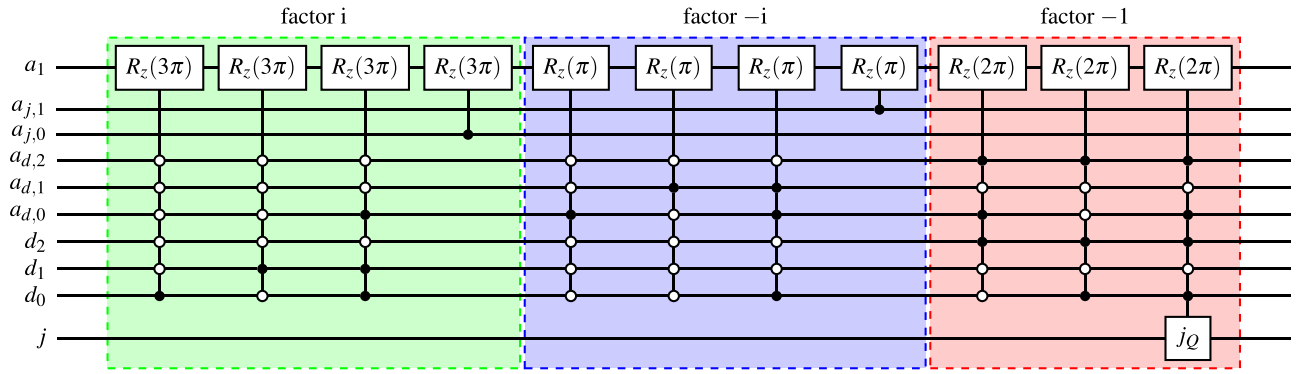

FIG. 12. Quantum circuit of the oracle O_{S,a_1}. The circuit is constructed according to Table III. Each colored box multiplies the amplitude stored in $|a_1\rangle$ by the factor specified in the figure (i, $-i$, -1). The rotation gate R_z acts as shown in Eq. (25).

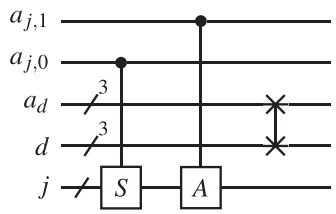

FIG. 13. Quantum circuit of the oracle O_M. The subtractor S and the adder A are shown in Fig. 14. The oracle converts the relative positions stored in the register $|a_j\rangle$ into the corresponding absolute positions and stores them in the register $|j\rangle$. Then, the circuit swaps the registers $|d\rangle$ and $|a_d\rangle$.

The total number of gates necessary to implement the whole polynomial scales as $\mathcal{O}(Dn_x^2)$.

C. Quantum measurements

In an actual quantum simulation, the output vector cannot be accessed directly. One can measure only the expectation value of a given operator on the output state. How to do this for potentially practical rf simulations is a problem separate from QSP that we discuss here, so it is left to future work. However, here is how at least one of the quantities of interest can be measured, namely, the wave energy within a given spatial volume.

The field components are encoded into the quantum state ψ as shown in Eq. (22). To compute the electric energy, one needs to sum the squares of the electric components in a desired spatial interval. As an example, a case with $n_x = 4$ is considered in Fig. 18. The QSP algorithm outputs ψ_{out} that encodes plasma variables if the QSP ancillae $|a_{\text{qsp}}\rangle$ are all in the zero state. In this example, we sum up $W_e = \tilde{E}_x^2 + \tilde{E}_y^2$ over the spatial points with indices $j = [2, \ldots, 5]$. The first controlled Pauli X gate entangles the superposition of the amplitudes of both $\tilde{E}_x(j \in [2, 3])$ and $\tilde{E}_y(j \in [2, 3])$ with the state $|1\rangle_{c_0}$. The second X gate entangles $\tilde{E}_x(j \in [4, 5])$ and $\tilde{E}_y(j \in [4, 5])$ with the state $|1\rangle_{c_1}$. The last controlled X gate finds the conjunction (logical AND) of the above states, and as a result, stores $\sum_{j=2}^{5} W_e(x_j)$ as the probability of the state $|1\rangle_m$.

If the qubit m has the state $|1\rangle$ with amplitude a, then it takes at least $\mathcal{O}(|a|^{-2})$ repetitions of the whole QSP operator before the direct measurement returns $|m\rangle = |1\rangle$. However, there is a quantum *amplitude-amplification* (AA) algorithm [51–53] that requires only $\mathcal{O}(|a|^{-1})$ iterations of the operator to measure the desired state with probability at least $\max(1 - |a|^2, |a|^2)$. This method is the basis of so-called *amplitude-estimation* (AE) techniques [53–56] that allow us to find the state probability with a predefined absolute error δ. The AA is based on the Grover-like [51,52] rotation R_{AA} in the quantum space spanned by a state of interest $|\text{G}\rangle$ ($\sim|1\rangle_m$ in our case) and a "garbage" state $|\text{B}\rangle$ ($\sim|0\rangle_m$) in such a way that the amplitude of the rotated state $|\text{G}\rangle$ becomes a sinusoidal function of the number of applications n_{AA} of R_{AA}: $\sin[(2n_{AA} + 1)\theta]$, where $\sin^2\theta = |a|^2$ and $\theta \in [0, \pi/2]$. In our case, every rotation includes the whole QSP operator and its inverse.

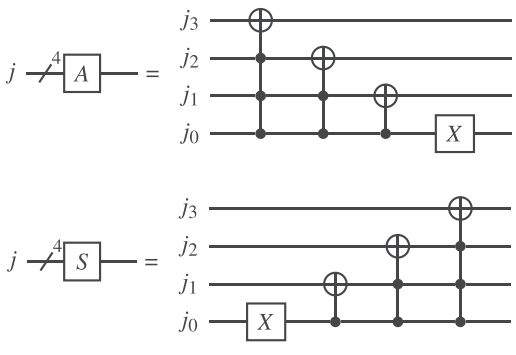

FIG. 14. Quantum circuits of the adder and of the subtractor by 1 for the case with four qubits.

As shown in Ref. [53], the operator R_{AA} has eigenvalues $\exp(\pm i2\theta)$. Therefore, one can calculate the probability $|a|^2$ from the estimation of the angle θ by constructing a superposition of states rotated with several n_{AA}, and by applying a subsequent *quantum Fourier transform* (QFT). That is the essence of the conventional AE algorithm described in Ref. [53]. This method estimates the probability $|a|^2$ with an absolute error δ by applying $M = \mathcal{O}(1/\delta)$ queries (in our case, calls to the QSP) and by using $\log_2(M)$ ancilla qubits, while classically one would need $\mathcal{O}(1/\delta^2)$ queries due to the central limit theorem. In our case, the error δ corresponds to the absolute error of the measured space-integrated energy. More details are given in Appendix C.

There are also state-of-the-art AE techniques [54–56] with a similar asymptotic scaling but smaller number of ancillae and controlled gates. For instance, the algorithm proposed in Ref. [54] also uses a set of AA operators with a various number of rotations R_{AA}. However, instead of the QFT, it performs statistical postprocessing of measurement results by implementing the maximum likelihood estimation of $|a|^2$.

The numerical implementation of the quantum measurements for classical rf systems is left to future work.

VII. DISCUSSION AND CONCLUSIONS

We have proposed how to apply the quantum signal processing (QSP) technique to simulating cold plasma waves and explicitly developed a quantum algorithm for modeling one-dimensional X-wave propagation in cold electron plasma. We have demonstrated how to construct an oracle to encode the wave Hamiltonian into a quantum circuit. The number of the ancillae in this oracle does not depend on the spatial resolution, so one can use a resolution higher than in the case with the standard state-preparation method. Since the oracle complexity scales as $\mathcal{O}(\text{poly}(\log_2 N_x))$, QSP simulations can provide a near-exponential speedup in comparison to classical simulations, which scale as $\mathcal{O}(N_x)$. This approach can be particularly helpful in simulations with high spatial resolution, which is advantageous, for example, for modeling the wave dynamics near resonances.

Our quantum simulations have been performed on a digital emulator of the quantum circuit and have shown agreement with the corresponding classical modeling. For emulation, we used the QuEST numerical toolkit [41] that operates with a whole 2^{n_q} state vector in a circuit with n_q qubits. For our one-dimensional QSP simulations, the emulator has shown

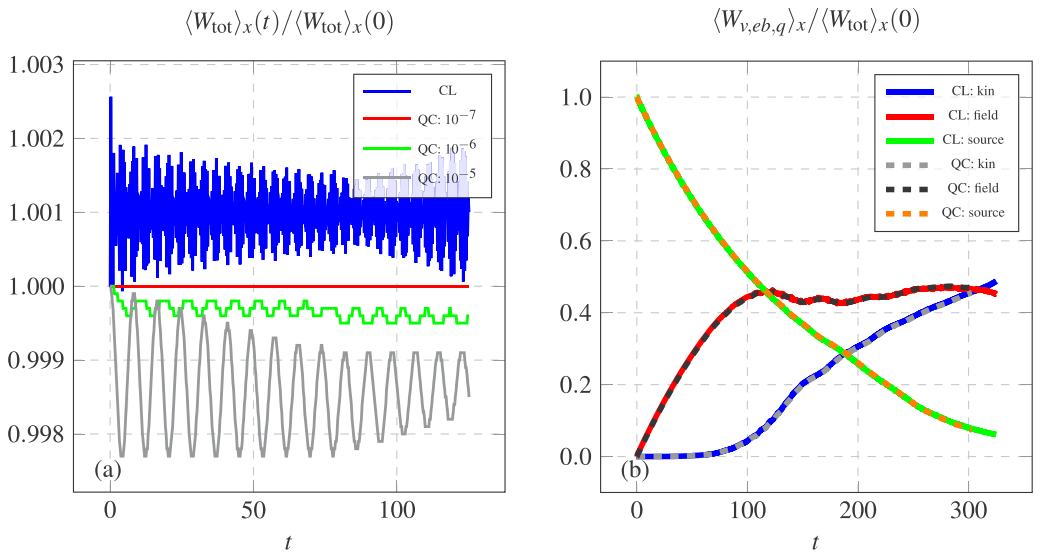

FIG. 15. (a) Space-integrated total system energy for different values of the QSP error $\varepsilon_{\rm qsp}$. (b) Comparison of the corresponding energy components [Eqs. (13a)–(13c)] in classical and quantum (with $\varepsilon_{\rm qsp} = 10^{-6}$) simulations. Here, CL stands for classical simulations and QC stands for emulated quantum simulations.

efficient parallelization on GPUs. However, one might need a more advanced emulator for higher-dimensional simulations. One of the promising approaches is the model proposed in Ref. [57]. It uses the fact that a quantum state is mostly sparse; i.e., many elements of the state vector are zero. If only its nonzero elements were stored (e.g., in the form of a hash table), one could significantly reduce memory usage and the simulation runtime. Moreover, one could model oracles with conditional rotations implemented via actual arithmetic functions with a big number of ancillae, since the ancillae act only locally and are zeroed otherwise thus being removed from the memory. Yet, this model needs to be extended with a GPU parallelization and the corresponding implementation of dynamic hash tables [58].

Based on our results, we can also assess the overall utility of the QSP technique in application to linear problems. Being a universal algorithm with a clear hierarchical structure, the QSP can be easily coded as a set of subsequent subroutines where only the block-encoding module needs to be modified for different plasma problems. The QSP provides an optimal dependence of the query complexity (the number of calls to the oracle) on the simulation time and on the error tolerance (as was pointed out in Ref. [34]). Also, the QSP requires only two ancillae in addition to the qubits used by the oracle. This reduces the circuit width. That said, the QSP circuits and our oracle in particular have many multicontrolled operators, where one gate is controlled by several nodes. Such a configuration is not directly realizable on existing quantum computers. The decomposition of these operators strongly depends on what gates are available on a chosen quantum computer, and on how the circuit is mapped on a specific quantum processor. Both of these aspects will

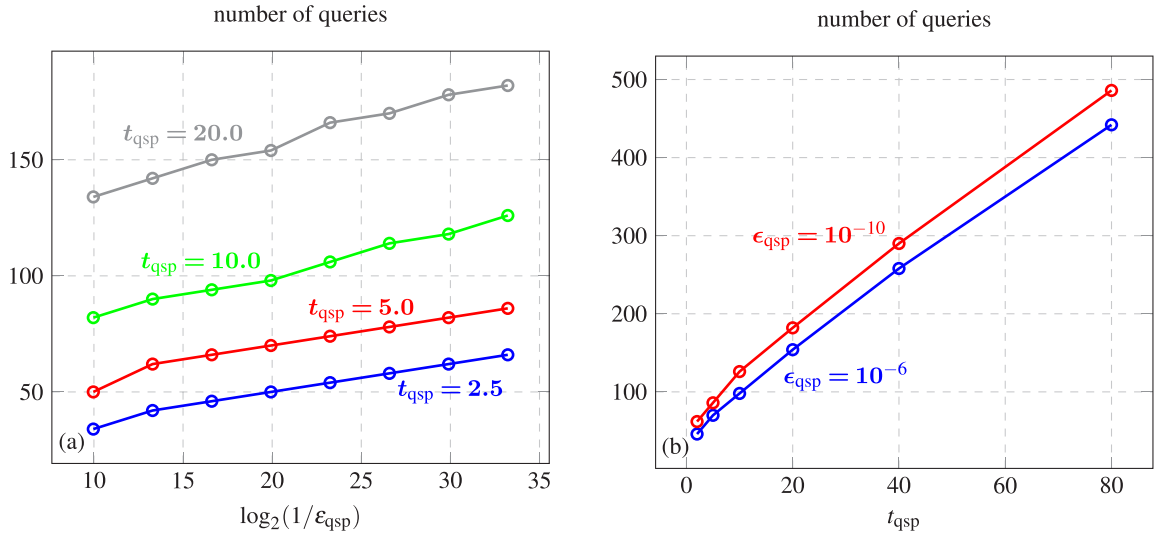

FIG. 16. Dependence of the query complexity on the QSP error $\varepsilon_{\rm qsp} \in [10^{-3}, 10^{-4}, \ldots, 10^{-10}]$ (a) and on the simulation time $t_{\rm qsp}$ (b).

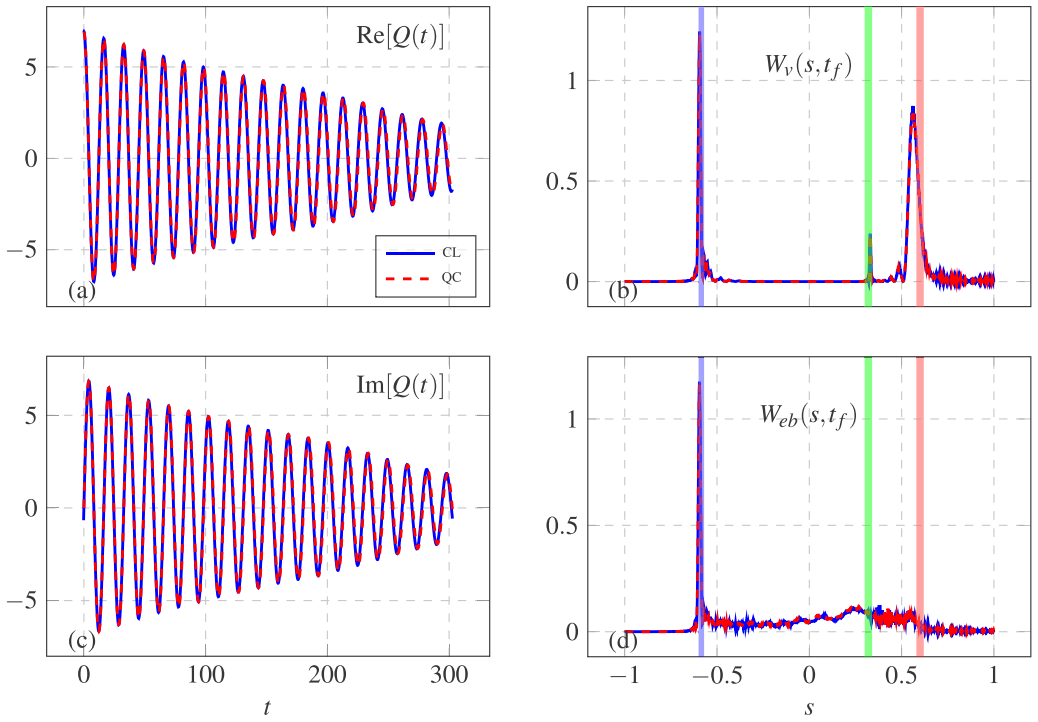

FIG. 17. Comparison of classical (solid blue curves) and emulated quantum (red dashed curves) simulations. Real (a) and imaginary (c) components of the source Q. (b) Kinetic energy W_v [Eq. (13a)] at time t_f as a function of s. (d) Field energy W_{eb} [Eq. (13b)] at time t_f as a function of s. The vertical lines show the HCR (blue), the LCR (green), the IUHR (red).

be hardware-dependent, so the limitations of the QSP will become clearer when practical error-corrected quantum computers with sufficiently many qubits become available. In general, an arbitrary single-target n_q-controlled gate can be decomposed into $\mathcal{O}(n_q^2)$ elementary gates by adding $\mathcal{O}(n_q)$ ancillae [48]. Another possibility is the hardware implementation of these gates. For example, a possible realization of an n-controlled iSWAP gate is proposed in Ref. [59]. Also, application of the so-called diamond gates, which are native in superconducting circuits, to reach higher connectivity in quantum circuits is discussed in Refs. [60,61].

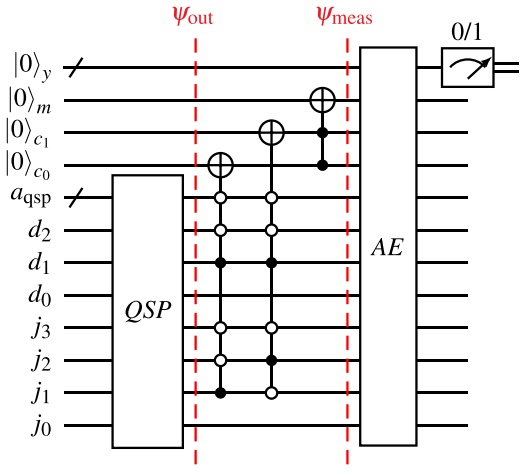

FIG. 18. Schematic circuit of the measurement of the electric energy density W_e summed over the spatial points with indices $j = [2, \ldots, 5]$, for $n_x = 4$. The register $|a_{qsp}\rangle$ represents all ancillae necessary for the QSP technique. The electric energy components are addressed using the control nodes on $|d\rangle = |2\rangle$ (for $\tilde{E}_x$) and $|d\rangle = |3\rangle$ (for $\tilde{E}_y$) [Eqs. (12) and (21)]. The resulting state is $\psi_{meas} = \sum_{k=2}^{5}[\tilde{E}_x(x_k)|2\rangle_d + \tilde{E}_y(x_k)|3\rangle_d]|k\rangle_j|1\rangle_m + \ldots|0\rangle_m$ (the other registers are omitted), where the desired information is stored in the probability amplitude of the state $|1\rangle_m$. Information about the state of the register m is then written to the register y by the AE (Appendix C).

Taking into account the block-encoding scaling with N_x, the dependence of the QSP circuit on the length of the simulated time interval t, and the number of the QSP queries needed for measurements, the final scaling of our circuit depth is

$$\mathcal{O}\left(\frac{\text{poly}(\log_2 N_x)}{\delta}[t_{qsp} + \log_2(1/\delta)]\right), \tag{45}$$

where we take the absolute error δ, which appears from measurements, equal to the QSP approximation error ε_{qsp}. The numerical coefficient in the scaling is determined by the specific implementation of the conditional rotations and of the measurement algorithm. Studying these subjects is left to future work.

Also note that the plasma model assumed in our paper is limited. One obvious limitation is that the waves are considered linear; but this is also true for most rf codes. A bigger limitation is that thermal effects and dissipation are neglected, including collisional and collisionless damping and also the possible wave-energy leaking through the boundaries of the simulation domain. (Remember that reflective boundary conditions are assumed in our algorithm.) Reinstating these effects makes the Hamiltonian in Eq. (3) non-Hermitian [11],

and then Hamiltonian simulations cannot be done using the QSP. A possible solution to this is to consider stationary waves ($\partial_t = -i\omega$) and solve the corresponding boundary-value problem, as commonly done in classical rf modeling. Instead of Hamiltonian simulations, solving a boundary-value problem requires only inverting a non-Hermitian matrix [11]. A possible way to do it is by using the known algorithm based on the quantum singular value transformation (QSVT) [35,38,62]. Because such simulations would be very different from those considered in this paper, we leave them to future work as well.

ACKNOWLEDGMENTS

The research described in this paper was conducted under the Laboratory Directed Research and Development (LDRD) Program at Princeton Plasma Physics Laboratory, a national laboratory operated by Princeton University for the U.S. Department of Energy under Prime Contract No. DE-AC02-09CH11466. The authors also thank Alexander Engel for valuable discussions.

APPENDIX A: BLOCK ENCODING BY STATE-PREPARATION METHOD

The block encoding U_H of a Hermitian operator $\mathscr{H}$ can be constructed by applying the state-preparation algorithm [34] as a product of two unitary matrices,

$$U_H = T_2^\dagger T_1, \tag{A1}$$

where

$$T_1 = \sum_j |\psi_j\rangle\langle 0|_a\langle j|_s, \tag{A2}$$

$$T_2 = \sum_k |\chi_k\rangle\langle 0|_a\langle k|_s. \tag{A3}$$

Each T_i involves the sum of states $|\psi\rangle$ and $|\chi\rangle$ defined as

$$|\psi_j\rangle = \sum_{p\in F_j} \frac{|p\rangle_{a_3}}{\sqrt{\varsigma}} |\mathscr{H}_{jp}\rangle_{a_1}|0\rangle_{a_2}|j\rangle_s, \tag{A4}$$

$$|\chi_k\rangle = \sum_{p\in F_k} \frac{|k\rangle_{a_3}}{\sqrt{\varsigma}} |\mathscr{H}_{kp}\rangle_{a_2}|0\rangle_{a_1}|p\rangle_s, \tag{A5}$$

where

$$|\mathscr{H}_{jk}\rangle_a = \sqrt{\frac{|\mathscr{H}_{jk}|}{M}}|0\rangle_a + \sqrt{1-\frac{|\mathscr{H}_{jk}|}{M}}|1\rangle_a. \tag{A6}$$

Using the oracle O_F [Eq. (43)], one finds a set of column indices F_j of all nonzero elements on the row j. The operator T_1 reads the row index j and saves the corresponding column indices to the ancilla register $|a_3\rangle$. After that, it rotates the ancilla qubit $|a_1\rangle$, so the necessary matrix element (its square root) becomes the amplitude of the zero state $|0\rangle_{a_1}$ [Eq. (A6)]. This is implemented by the oracle $O_{\sqrt{H}}$ in Eq. (43). The operator T_2 rotates the ancilla qubit $|a_2\rangle$ in a similar way by taking a row index from the ancilla register $|a_3\rangle$ and column indices from the register $|s\rangle$. Since the encoding of the row and column indices in the registers a_3 and s in $|\chi_k\rangle$ is swapped in comparison with the state $|\psi_j\rangle$, we introduce the oracle O_M, which performs the corresponding index swapping in Eq. (43).

APPENDIX B: TABULAR DESCRIPTION OF THE ORACLE CIRCUITS

In Tables I, II, and III, one can find the descriptions of the various oracles whose circuits are shown in Sec. V. The action of each oracle is defined by a set of output states, which should be returned by the oracle for the indicated input states. The notations of the main and ancilla registers (d, a_d, etc.) coincide with those introduced in Secs. III D and V C. Together, the tables describe the Hamiltonian (17).

TABLE I. Action of the oracle O_F. An input variable is encoded into the register $|d\rangle$, and its space dependence is taken from the register $|j\rangle$. The operator O_F returns the registers $|a_j\rangle|a_d\rangle$ in the indicated output states, while the states of the registers $|d\rangle|j\rangle$ remain unchanged.

Variable	Input[a]	Output
ξ_x	$\|000\rangle_d\|j\rangle_j$	$\|00\rangle_{a_j}\|001\rangle_{a_d} + \|00\rangle_{a_j}\|010\rangle_{a_d}$
ξ_y	$\|001\rangle_d\|0;N_x-1\rangle_j$	$\|00\rangle_{a_j}\|000\rangle_{a_d}$
	$\|001\rangle_d\|[1,N_x-2]\rangle_j$	$\|00\rangle_{a_j}\|000\rangle_{a_d} + \|00\rangle_{a_j}\|011\rangle_{a_d}$
$\tilde{E}_x$	$\|010\rangle_d\|j\rangle_j$	$\|00\rangle_{a_j}\|000\rangle_{a_d}$
$\tilde{E}_y$	$\|011\rangle_d\|0;N_x-1\rangle_j$	$\|00\rangle_{a_j}\|011\rangle_{a_d}$
	$\|011\rangle_d\|1\rangle_j$	$\|00\rangle_{a_j}\|001\rangle_{a_d} + \|10\rangle_{a_j}\|100\rangle_{a_d}$
	$\|011\rangle_d\|[2,N_x-3]\rangle_j$	$\|00\rangle_{a_j}\|001\rangle_{a_d} + \|01\rangle_{a_j}\|100\rangle_{a_d} + \|10\rangle_{a_j}\|100\rangle_{a_d}$
	$\|011\rangle_d\|N_x-2\rangle_j$	$\|00\rangle_{a_j}\|001\rangle_{a_d} + \|01\rangle_{a_j}\|100\rangle_{a_d}$
$\tilde{B}_z$	$\|100\rangle_d\|0;N_x-1\rangle_j$	$\|00\rangle_{a_j}\|100\rangle_{a_d}$
	$\|100\rangle_d\|1\rangle_j$	$\|10\rangle_{a_j}\|011\rangle_{a_d}$
	$\|100\rangle_d\|[2,N_x-3]\neq j_Q\rangle_j$	$\|01\rangle_{a_j}\|011\rangle_{a_d} + \|10\rangle_{a_j}\|011\rangle_{a_d}$
	$\|100\rangle_d\|j_Q\rangle_j$	$\|01\rangle_{a_j}\|011\rangle_{a_d} + \|10\rangle_{a_j}\|011\rangle_{a_d} + \|00\rangle_{a_j}\|101\rangle_{a_d}$
	$\|100\rangle_d\|N_x-2\rangle_j$	$\|01\rangle_{a_j}\|011\rangle_{a_d}$
Q	$\|101\rangle_d\|j\neq j_Q\rangle_j$	$\|00\rangle_{a_j}\|101\rangle_{a_d}$
	$\|101\rangle_d\|j_Q\rangle_j$	$\|00\rangle_{a_j}\|100\rangle_{a_d} + \|00\rangle_{a_j}\|101\rangle_{a_d}$

[a] $|0;N_x-1\rangle_j$ denotes $|0\rangle_j$ or $|N_x-1\rangle_j$ states; $|[1,N_x-2]\rangle_j$ denotes all states from $|1\rangle_j$ up to $|N_x-2\rangle_j$; $|j_Q\rangle_j$ corresponds to the spatial position of the source Q.

TABLE II. Action of the oracle $O_{\sqrt{H}}$. The operator is controlled by the indicated input registers. For various bit arrays encoded in these registers, it returns the indicated output amplitudes on the ancilla a_1 (or a_2) as explained in Eq. (37).

Input	Output amplitude
$\|001\rangle_{a_d}\|000\rangle_d$	$\sqrt{\beta_H B_0}$
$\|000\rangle_{a_d}\|001\rangle_d$	$\sqrt{\beta_H B_0}$
$\|010\rangle_{a_d}\|000\rangle_d$	$\sqrt{\beta_H n_0^{1/2}}$
$\|011\rangle_{a_d}\|001\rangle_d$	$\sqrt{\beta_H n_0^{1/2}}$
$\|000\rangle_{a_d}\|010\rangle_d$	$\sqrt{\beta_H n_0^{1/2}}$
$\|001\rangle_{a_d}\|011\rangle_d$	$\sqrt{\beta_H n_0^{1/2}}$
$\|01\rangle_{a_j}$	$\sqrt{\beta_H/(2h)}$
$\|10\rangle_{a_j}$	$\sqrt{\beta_H/(2h)}$
$\|101\rangle_{a_d}\|100\rangle_d$	$\sqrt{\beta_H\beta}$
$\|100\rangle_{a_d}\|101\rangle_d$	$\sqrt{\beta_H\beta}$
$\|101\rangle_{a_d}\|101\rangle_d$	$\sqrt{\beta_H\omega_a}$

One can consider Table I as a set of instructions. Each instruction says which column indices encoded in the ancilla registers a_j and a_d should be returned by the oracle O_F, when the oracle is initialized with a row index encoded in the main registers d and j. In other words, this table indicates where nonzero matrix elements sit inside the Hamiltonian. According to Eq. (17), several rows of the Hamiltonian have only zero elements. In this case, to simplify the construction of the oracle O_F, we output the column index equal to the row index, as one can see, for instance, for the input $|101\rangle_d|j \neq j_Q\rangle_j$ (in the block Q) in Table I. The presence of these diagonal elements does not affect the action of the oracles $O_{\sqrt{H}}$ and O_S.

Table II presents the square roots of the absolute values of the matrix elements given the element row and column indices. The sign and the additional unitary factor i contained in these elements are presented in Table III.

To create the $O_{\sqrt{H}}$ quantum circuit, we use gates that perform rotations $R_y(\theta_j)$ conditioned on the register j. Every combination of qubits in $|j\rangle$ corresponds to a particular angle θ_j expressing the space dependence of a given field on x. For instance, to obtain the profile of the background magnetic field, one can use angles $\theta_j = 2\arccos\sqrt{\beta_H B_{0,j}}$. For convenience, we denote the corresponding conditional gate as $R(B)$ in our quantum circuit (Fig. 11).

TABLE III. Action of the oracle O_{S,a_1}. For a given indicated state, the operator outputs the corresponding coefficient that is multiplied by the value returned by the oracle $O_{\sqrt{H},a_1}$.

Input	Output multiplier
$\|000\rangle_{a_d}\|001\rangle_d$	i
$\|000\rangle_{a_d}\|010\rangle_d$	i
$\|001\rangle_{a_d}\|011\rangle_d$	i
$\|01\rangle_{a_j}$	i
$\|001\rangle_{a_d}\|000\rangle_d$	$-i$
$\|010\rangle_{a_d}\|000\rangle_d$	$-i$
$\|011\rangle_{a_d}\|001\rangle_d$	$-i$
$\|10\rangle_{a_j}$	$-i$
$\|101\rangle_{a_d}\|100\rangle_d$	-1
$\|100\rangle_{a_d}\|101\rangle_d$	-1
$\|101\rangle_{a_d}\|101\rangle_d$	-1

The conditional-rotation gates must be expressed via arithmetic functions with a set of additional qubits to store the angles θ_j. In our work, every conditional gate is coded as a multiqubit gate with inner subblocks as in Eq. (36) on the main diagonal. Every subblock corresponds to one θ_j for a particular j. The circuit depth of $O_{\sqrt{H}}$ may strongly depend on how efficient the implementation of the conditional gates is for given profiles and how they depend on the system size N_x. However, the general tendency is that the depth of quantum arithmetic circuits scales as $\mathcal{O}(\text{poly}(n_x))$ (Refs. [1,50]).

According to Eq. (28), the normalization of the Hamiltonian depends on the matrix sparsity. This dependence is reflected in the fact that d_H^2 appears in the normalization coefficient β_H in Eq. (39). In our case, $d_H^2 = 4$, which is close to the sparsity $\varsigma = 3$ of our wave Hamiltonian [Eq. (17)], as it should be according to Eq. (26). If $\varsigma > 1$, then one must encode the positions of several nonzero elements knowing only a single row index. This means that a superposition of several quantum states has to be created from a single input state. For instance, the input state $|011\rangle_d|1\rangle_j$ must create a superposition of two states, $|00\rangle_{a_j}|001\rangle_{a_d} + |10\rangle_{a_j}|100\rangle_{a_d}$. This can be done by applying a Hadamard gate, and one needs at least $n_H = 2$ Hadamard gates to produce the superposition of $\varsigma = 3$ states. However, the amplitude of each state in the resulting superposition has an additional multiplier $1/2^{n_H/2}$. Then, according to Eq. (37), we encode the square root of the absolute value of the matrix element v as

$$\sqrt{\frac{|v|}{d_H^2 M}} = \frac{1}{2^{n_H/2}}\cos(\theta/2), \tag{B1}$$

where $\cos(\theta/2) = \sqrt{|v|/M} \leqslant 1$, and therefore, $d_H = 2^{n_H/2}$.

APPENDIX C: AMPLITUDE ESTIMATION

As shown in Fig. 18, we can store the energy integrated over a given spatial volume as the probability p_G of the state $|1\rangle$ on the ancilla qubit m:

$$\psi_{\text{meas}} = a_B|0\rangle + a|1\rangle, \tag{C1a}$$

$$p_G \equiv |a|^2 = \langle W\rangle_x(t_f), \tag{C1b}$$

$$p_B \equiv |a_B|^2 = 1 - p_G. \tag{C1c}$$

To save the energy in the ancilla m, we perform the postselection by choosing only those states where all QSP ancillae qubits are in the zero state. If we calculate the total system energy, the resulting probability of the postselected state will be close to unity, $p_G \approx 1$, with an absolute error defined by the QSP approximation error ε_{qsp}. However, if we want to find an energy component in a small spatial volume, then the corresponding probability can be much less than unity,

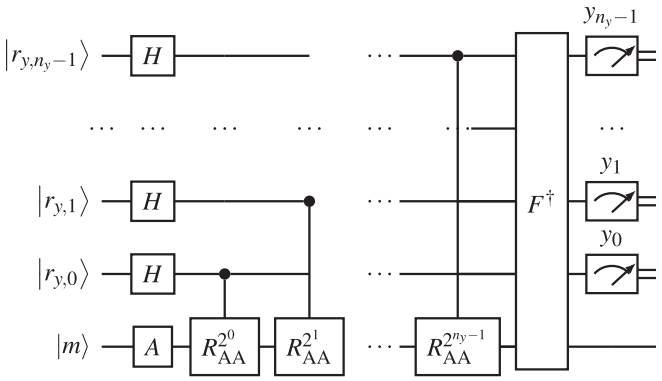

FIG. 19. Circuit for the amplitude estimation. Here, $F^\dagger$ is the inverse quantum Fourier transform. The circuit for the Fourier transform, F, can be found in Ref. [30]. Here, as in the rest of the paper, it is assumed that the top qubit is the most significant one.

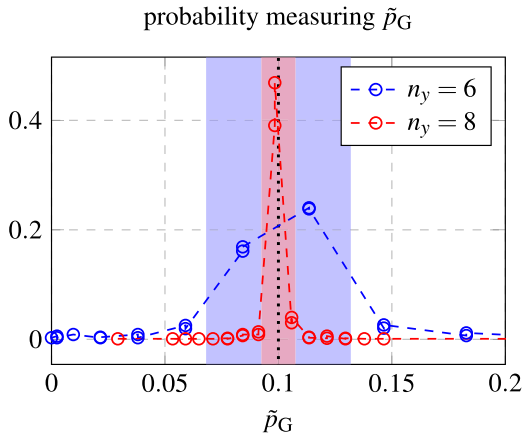

FIG. 20. Probability distribution of measurement outcomes $\tilde{p}_G$. Amplitude estimation of known $p_G = 0.1$ is performed with $n_y = 6$ (blue markers) and $n_y = 8$ (red markers). The shaded areas mark the corresponding theoretical intervals presented in Eq. (C5).

$p_G \ll 1$. Once the state ψ_{meas} is formed, one can use the amplitude estimation (AE) technique to measure p_G.

There is a wide variety of modern AE techniques as has been discussed in Sec. VI C. Here, however, we use the standard AE first introduced in Ref. [53] to show how the $1/\delta$ factor appears in the final scaling of our circuit, Eq. (45). For any AE method, we need an operator A that creates the state whose probability p_G we need to measure. In Hamiltonian simulations, A is equal to the product of the QSP operator and of the energy integration over a given spatial volume.

The value p_G can be changed by using the amplitude-amplification (AA) operator R_{AA}:

$$R_{AA} = AS_0A^\dagger S_G, \tag{C2a}$$

$$S_0 = 1 - 2|0\rangle_m\langle 0|_m, \tag{C2b}$$

$$S_G = 1 - 2|1\rangle_m\langle 1|_m, \tag{C2c}$$

where the operator S_0 inverses the sign of the initial state, which is $|0\rangle_m$; the operator S_G inverses the sign of the state to measure, which is $|1\rangle_m$ in our case. To find p_G, we need to estimate the eigenphase $2\theta_B$ of the operator R_{AA}. This can be done by using the phase estimation circuit as shown in Fig. 19. The circuit requires $\sum_{k=0}^{n_y-1} 2^k = M - 1$ queries to R_{AA}, where $M = 2^{n_y}$. This results in $\mathcal{O}(M)$ requests to the oracle A. More precisely, one needs M queries to A and $M - 1$ queries to $A^\dagger$ to perform the AE. The eigenphase is then calculated by using the following integer:

$$y = \sum_{k=0}^{n_y-1} y_k 2^k, \tag{C3}$$

where each $y_k = 0$ or 1 is measured on the corresponding qubit $r_{y,k}$. The resulting phase and the corresponding probability are estimated as

$$\theta_B = \frac{\pi y}{2^{n_y}}, \tag{C4a}$$

$$\tilde{p}_B = \sin^2(\theta_B). \tag{C4b}$$

After that, one can estimate p_G by using Eq. (C1c). With a probability not less than $8/\pi^2 \approx 0.81$, the absolute error of the estimation is [53]

$$\delta \equiv |p_G - \tilde{p}_G| \leqslant 2\pi \frac{\sqrt{p_G(1-p_G)}}{M} + \frac{\pi^2}{M^2}. \tag{C5}$$

This means that $\delta = \mathcal{O}(1/M)$, which results in $\mathcal{O}(1/\delta)$ queries to the oracle A in the AE circuit. As mentioned above, in the general case of QSP simulations, the oracle A includes the whole QSP circuit. Therefore, to calculate p_G, we need $\mathcal{O}(1/\delta)$ requests to the QSP operator. This explains the appearance of the prefactor $\mathcal{O}(1/\delta)$ in the final scaling (45). As an example, numerical estimation of $p_G = 0.1$ is given in Fig. 20 for two different n_y.

[1] A. Suau, G. Staffelbach, and H. Calandra, Practical quantum computing, ACM Trans. Quantum Comput. **2**, 1 (2021).

[2] Y. Cao, A. Papageorgiou, I. Petras, J. Traub, and S. Kais, Quantum algorithm and circuit design solving the Poisson equation, New J. Phys. **15**, 013021 (2013).

[3] S. Wang, Z. Wang, W. Li, L. Fan, Z. Wei, and Y. Gu, Quantum fast Poisson solver: The algorithm and complete and modular circuit design, Quantum Inf. Process. **19**, 170 (2020).

[4] S. Sinha and P. Russer, Quantum computing algorithm for electromagnetic field simulation, Quantum Inf. Process. **9**, 385 (2010).

[5] A. Scherer, B. Valiron, S.-C. Mau, S. Alexander, E. van den Berg, and T. E. Chapuran, Concrete resource analysis of the quantum linear-system algorithm used to compute the electromagnetic scattering cross section of a 2D target, Quantum Inf. Process. **16**, 60 (2017).

[6] F. Fillion-Gourdeau and E. Lorin, Simple digital quantum algorithm for symmetric first-order linear hyperbolic systems, Numer. Alg. **82**, 1009 (2019).

[7] F. Gaitan, Finding flows of a Navier-Stokes fluid through quantum computing, npj Quantum Inf. **6**, 61 (2020).

[8] F. Gaitan, Finding solutions of the Navier-Stokes equations through quantum computing-recent progress, a generalization, and next steps forward, Adv. Quantum Technol. **4**, 2100055 (2021).

[9] B. N. Todorova and R. Steijl, Quantum algorithm for the collisionless Boltzmann equation, J. Comput. Phys. **409**, 109347 (2020).

[10] L. Budinski, Quantum algorithm for the advection-diffusion equation simulated with the lattice Boltzmann method, Quantum Inf. Process. **20**, 57 (2021).

[11] I. Y. Dodin and E. A. Startsev, On applications of quantum computing to plasma simulations, Phys. Plasmas **28**, 092101 (2021).

[12] T. H. Stix, *Waves in Plasmas* (AIP Press, Melville, NY, 1992).

[13] R. I. Pinsker, Introduction to wave heating and current drive in magnetized plasmas, Phys. Plasmas **8**, 1219 (2001).

[14] R. Prater, Heating and current drive by electron cyclotron waves, Phys. Plasmas **11**, 2349 (2004).

[15] N. J. Fisch, Theory of current drive in plasmas, Rev. Mod. Phys. **59**, 175 (1987).

[16] N. J. Fisch, Confining a Tokamak Plasma with rf-Driven Currents, Phys. Rev. Lett. **41**, 873 (1978).

[17] N. J. Fisch and A. H. Boozer, Creating an Asymmetric Plasma Resistivity with Waves, Phys. Rev. Lett. **45**, 720 (1980).

[18] A. H. Reiman, Suppression of magnetic islands by rf driven currents, Phys. Fluids **26**, 1338 (1983).

[19] A. H. Reiman and N. J. Fisch, Suppression of Tearing Modes by Radio Frequency Current Condensation, Phys. Rev. Lett. **121**, 225001 (2018).

[20] B. J. Ding, P. T. Bonoli, A. Tuccillo, M. Goniche, K. Kirov, M. Li, Y. Li, R. Cesario, Y. Peysson, A. Ekedahl, L. Amicucci, S. Baek, I. Faust, R. Parker, S. Shiraiwa, G. M. Wallace, A. Cardinali, C. Castaldo, S. Ceccuzzi, J. Mailloux *et al.*, Review of recent experimental and modeling advances in the understanding of lower hybrid current drive in ITER-relevant regimes, Nucl. Fusion **58**, 095003 (2018).

[21] T. I. Tsujimura, R. Yanai, Y. Mizuno, K. Tanaka, Y. Yoshimura, T. Tokuzawa, M. Nishiura, R. Sakamoto, G. Motojima, S. Kubo, T. Shimozuma, H. Igami, H. Takahashi, M. Yoshinuma, and S. Ohshima, Improved performance of electron cyclotron resonance heating by perpendicular injection in the Large Helical Device, Nucl. Fusion **61**, 026012 (2021).

[22] P. T. Bonoli and M. Porkolab, Radiofrequency current generation by lower hybrid slow waves in the presence of fusion generated alpha particles in the reactor regime, Nucl. Fusion **27**, 1341 (1987).

[23] R. Cesario, L. Amicucci, A. Cardinali, C. Castaldo, M. Marinucci, L. Panaccione, F. Santini, O. Tudisco, M. L. Apicella, G. Calabrò, C. Cianfarani, D. Frigione, A. Galli, G. Mazzitelli, C. Mazzotta, V. Pericoli, G. Schettini, A. A. Tuccillo, B. Angelini, G. Apruzzese *et al.*, Current drive at plasma densities required for thermonuclear reactors, Nat. Commun. **1**, 55 (2010).

[24] B. N. Wan, Y. Liang, X. Z. Gong, N. Xiang, G. S. Xu, Y. Sun, L. Wang, J. P. Qian, H. Q. Liu, L. Zeng, L. Zhang, X. J. Zhang, B. J. Ding, Q. Zang, B. Lyu, A. M. Garofalo, A. Ekedahl, M. H. Li, F. Ding, S. Y. Ding *et al.*, Recent advances in EAST physics experiments in support of steady-state operation for ITER and CFETR, Nucl. Fusion **59**, 112003 (2019).

[25] G. M. Wallace, B. J. Ding, M. H. Li, J. Chen, S. G. Baek, P. T. Bonoli, S. Shiraiwa, L. Liu, and C. Wu, Scoping study of lower hybrid current drive for CFETR, Nucl. Fusion **61**, 106009 (2021).

[26] A. Fasoli, S. Brunner, W. A. Cooper, J. P. Graves, P. Ricci, O. Sauter, and L. Villard, Computational challenges in magnetic-confinement fusion physics, Nat. Phys. **12**, 411 (2016).

[27] V. A. Svidzinski, J. S. Kim, L. Zhao, S. A. Galkin, and J. A. Spencer, Hybrid iterative approach for simulation of radio-frequency fields in plasma, Phys. Plasmas **25**, 082509 (2018).

[28] E. R. Tracy, A. J. Brizard, A. S. Richardson, and A. N. Kaufman, *Ray Tracing and Beyond: Phase Space Methods in Plasma Wave Theory* (Cambridge University Press, New York, 2014).

[29] For example, see the recent series of Refs. [63–67] and the references cited therein.

[30] M. A. Nielsen and I. L. Chuang, *Quantum Computation and Quantum Information*, 10th anniversary ed. (Cambridge University Press, Cambridge, 2010).

[31] E. G. Rieffel and W. H. Polak, *Quantum Computing: A Gentle Introduction*, 1st ed. (MIT Press, Cambridge, MA, 2011).

[32] Circuit depth explanation: "Step 3. Interpret the result" at https://qiskit.org/textbook/ch-labs/Lab01_QuantumCircuits.html.

[33] G. H. Low and I. L. Chuang, Optimal Hamiltonian Simulation by Quantum Signal Processing, Phys. Rev. Lett. **118**, 010501 (2017).

[34] G. H. Low and I. L. Chuang, Hamiltonian simulation by qubitization, Quantum **3**, 163 (2019).

[35] A. Gilyén, Y. Su, G. H. Low, and N. Wiebe, Quantum singular value transformation and beyond: Exponential improvements for quantum matrix arithmetics, in *Proceedings of the 51st Annual ACM SIGACT Symposium on Theory of Computing*, STOC 2019 (ACM Press, New York, 2019), pp. 193–204.

[36] J. Haah, Product decomposition of periodic functions in quantum signal processing, Quantum **3**, 190 (2019).

[37] R. Chao, D. Ding, A. Gilyen, C. Huang, and M. Szegedy, Finding angles for quantum signal processing with machine precision, arXiv:2003.02831.

[38] Y. Dong, X. Meng, K. B. Whaley, and L. Lin, Efficient phase-factor evaluation in quantum signal processing, Phys. Rev. A **103**, 042419 (2021).

[39] V. von Burg, G. H. Low, T. Häner, D. S. Steiger, M. Reiher, M. Roetteler, and M. Troyer, Quantum computing enhanced computational catalysis, Phys. Rev. Research **3**, 033055 (2021).

[40] A. Engel, G. Smith, and S. E. Parker, Quantum algorithm for the Vlasov equation, Phys. Rev. A **100**, 062315 (2019).

[41] T. Jones, A. Brown, I. Bush, and S. C. Benjamin, QuEST and high performance simulation of quantum computers, Sci. Rep. **9**, 10736 (2019).

[42] D. G. Swanson, *Plasma Waves*, 2nd ed. (IOP, Philadelphia, 2003).

[43] For an introduction on the geometrical-optics approximation, see, for example, Refs. [12,28] or Secs. 7.1– 7.3 in I. Y. Dodin, arXiv:2201.08562 [J. Plasma Phys. (to be published)].

[44] G. H. Low, T. J. Yoder, and I. L. Chuang, Methodology of Resonant Equiangular Composite Quantum Gates, Phys. Rev. X **6**, 041067 (2016).

[45] J. M. Martyn, Y. Liu, Z. E. Chin, and I. L. Chuang, Efficient fully-coherent Hamiltonian simulation, arXiv:2110.11327.

[46] Computation of angles for quantum signal processing in F#, https://github.com/microsoft/Quantum-NC/tree/main/src/simulation/qsp.

[47] Efficient phase-factor evaluation in quantum signal processing: code, https://github.com/qsppack/QSPPACK.

[48] A. Barenco, C. H. Bennett, R. Cleve, D. P. DiVincenzo, N. Margolus, P. Shor, T. Sleator, J. A. Smolin, and H. Weinfurter, Elementary gates for quantum computation, Phys. Rev. A **52**, 3457 (1995).

[49] Numerical QSP framework implemented in C++, https://github.com/ivanNovikau/QSVT_framework.

[50] T. Häner, M. Roetteler, and K. M. Svore, Optimizing quantum circuits for arithmetic, arXiv:1805.12445.

[51] L. K. Grover, Quantum Mechanics Helps in Searching for a Needle in a Haystack, Phys. Rev. Lett. **79**, 325 (1997).

[52] L. K. Grover, Quantum Computers Can Search Rapidly by Using Almost Any Transformation, Phys. Rev. Lett. **80**, 4329 (1998).

[53] G. Brassard, P. Høyer, M. Mosca, and A. Tapp, Quantum amplitude amplification and estimation, Quantum Comput. Inf. **305**, 53 (2002).

[54] Y. Suzuki, S. Uno, R. Raymond, T. Tanaka, T. Onodera, and N. Yamamoto, Amplitude estimation without phase estimation, Quantum Inf. Process. **19**, 75 (2020).

[55] S. Uno, Y. Suzuki, K. Hisanaga, R. Raymond, T. Tanaka, T. Onodera, and N. Yamamoto, Modified Grover operator for quantum amplitude estimation, New J. Phys. **23**, 083031 (2021).

[56] D. Grinko, J. Gacon, C. Zoufal, and S. Woerner, Iterative quantum amplitude estimation, npj Quantum Inf. **7**, 52 (2021).

[57] S. Jaques and T. Häner, Leveraging state sparsity for more efficient quantum simulations, arXiv:2105.01533.

[58] Y. Li, Q. Zhu, Z. Lyu, Z. Huang, and J. Sun, DyCuckoo: Dynamic hash tables on GPUs, in *Proceedings of the 2021 IEEE 37th International Conference on Data Engineering (ICDE)* (IEEE Computer Society, Los Alamitos, CA, 2021), pp. 744–755.

[59] S. E. Rasmussen and N. T. Zinner, Simple implementation of high fidelity controlled-*i*swap gates and quantum circuit exponentiation of non-Hermitian gates, Phys. Rev. Research **2**, 033097 (2020).

[60] N. J. S. Loft, M. Kjaergaard, L. B. Kristensen, C. K. Andersen, T. W. Larsen, S. Gustavsson, W. D. Oliver, and N. T. Zinner, Quantum interference device for controlled two-qubit operations, npj Quantum Inf. **6**, 47 (2020).

[61] E. Bahnsen, S. Rasmussen, N. Loft, and N. Zinner, Application of the Diamond Gate in Quantum Fourier Transformations and Quantum Machine Learning, Phys. Rev. Applied **17**, 024053 (2022).

[62] J. M. Martyn, Z. M. Rossi, A. K. Tan, and I. L. Chuang, Grand unification of quantum algorithms, PRX Quantum **2**, 040203 (2021).

[63] I. Y. Dodin, D. E. Ruiz, K. Yanagihara, Y. Zhou, and S. Kubo, Quasioptical modeling of wave beams with and without mode conversion. I. Basic theory, Phys. Plasmas **26**, 072110 (2019).

[64] K. Yanagihara, I. Y. Dodin, and S. Kubo, Quasioptical modeling of wave beams with and without mode conversion. II. Numerical simulations of single-mode beams, Phys. Plasmas **26**, 072111 (2019).

[65] K. Yanagihara, I. Y. Dodin, and S. Kubo, Quasioptical modeling of wave beams with and without mode conversion. III. Numerical simulations of mode-converting beams, Phys. Plasmas **26**, 072112 (2019).

[66] K. Yanagihara, I. Y. Dodin, and S. Kubo, Quasioptical modeling of wave beams with and without mode conversion. IV. Numerical simulations of waves in dissipative media, Phys. Plasmas **28**, 122102 (2021).

[67] K. Yanagihara, S. Kubo, I. Y. Dodin, and the LHD Experiment Group, Quasioptical propagation and absorption of electron cyclotron waves: Simulations and experiment, Nucl. Fusion **61**, 106012 (2021).